Assessment of the Use of Prompt Gamma Emission for Proton Therapy Range Verification

By

John R Styczynski

Submitted to the Department of Nuclear Science and Engineering
in Partial Fulfillment of the Requirements for the Degrees of

Master of Science in Nuclear Science and Engineering
And
Bachelor of Science in Nuclear Science and Engineering
at the

Massachusetts Institute of Technology

June 2009

ARCHIVES

MASSACHUSETTS INSTITUTE OF TECHNOLOGY
AUG 19 2009
LIBRARIES

©2009 Massachusetts Institute of Technology
All rights reserved

Signature of Author _____

John R. Styczynski
Department of Nuclear Science and Engineering
15 May 2009

Certified by _____

Richard C. Lanza
Senior Research Scientist in Nuclear Science and Engineering, MIT
Thesis Supervisor

Certified by _____

Harald Paganetti
Associate Professor of Radiation Oncology, Massachusetts General Hospital
Thesis Reader

Certified by _____

Jacquelyn C. Yanch
Professor in Nuclear Science and Engineering, MIT
Thesis Reader

Accepted by _____

Jacquelyn C. Yanch
Professor in Nuclear Science and Engineering
Chair, Department Committee on Graduate Students

ASSESSMENT OF THE USE OF PROMPT GAMMA EMISSION FOR PROTON THERAPY RANGE VERIFICATION

Submitted to the Department of Nuclear Science and Engineering on 15 May 2009 in Partial Fulfillment of the Requirements for the Degrees of Master of Science in Nuclear Science and Engineering and Bachelor of Science in Nuclear Science and Engineering

ABSTRACT

PURPOSE: Prompt gamma rays emitted from proton-nucleus interactions in tissue present a promising non-invasive, *in situ* means of monitoring proton beam based radiotherapy. This study investigates the fluence and energy distribution of prompt gamma rays emitted during proton irradiation of phantoms. This information was used to develop a correlation between the measured and calculated gamma emission and the proton beam range, which would allow treatments to more effectively exploit the sharp distal falloff in the dose distributions of protons.
METHOD & MATERIALS: A model of a cylindrical Lucite phantom with a monoenergetic proton beam and an annular array of ideal photon tallies arranged orthogonal to the beam was developed using the Monte Carlo code MCNPX 2.6.0. Heterogeneous geometries were studied by inserting metal implants into the Lucite phantom, and simulating a phantom composed of bone and lung equivalent materials and polymethyl methacrylate.
RESULTS: Experimental and computational results indicated a correlation between gamma emission and the proton depth-dose profile. Several peaks were evident in the calculated energy spectrum and the 4.44 MeV emission from ^{12}C was the most intense line having any apparent correlation with the depth dose profile. Arbitrary energy binning of 4-5 MeV and 4-8 MeV was performed on the Monte Carlo data; this binned data yielded a distinct emission peak 1cm proximal to the Bragg peak. In all cases in the Lucite phantom the position of the Bragg peak's 80% distal falloff corresponded with the position of the 4-8MeV binned 50% distal falloff. The 4-5MeV binning strategy was successful with the heterogeneous phantom in which the proton beam entered lung and stopped in bone. However, the density disparity between the bone and lung equivalent materials rendered this technique unsuccessful for the heterogeneous phantom in which the beam entered bone and stopped in lung. For this 1.4MeV binning was conducted, assessing the 1.37 MeV characteristic gamma peak of ^{24}Mg, which was only present in the lung slab.
CONCLUSIONS: The results are promising and indicate the feasibility of prompt gamma emission detection as a means of characterizing the proton beam range *in situ*. This study has established the measurement and computational tools necessary to pursue the development of this technique.

Thesis Supervisor: Richard C. Lanza
Title: Senior Research Scientist in Nuclear Science and Engineering

ACKNOWLEDGEMENTS

I would like to thank Harald Paganetti and Thomas Bortfeld, without whom this project would have never come to fruition. Richard Lanza for his patience, guidance, and insight over the past five years. Peter Biggs, David Gierga, Andrew Hodgdon, and Jackie Yanch, who, over countless hours, have provided their generous insight into the development of MCNP models. Erik Johnson and Clare Egan who were always willing to help guide me through the ins and outs of MIT.

All of my friends, both in Boston and back home, you've been a much needed source of distraction during these past few years.

And, most importantly, my family. Without your love and support I wouldn't be where I am or who I am today.

TABLE OF CONTENTS

TABLE OF FIGURES

LIST OF TABLES

1 INTRODUCTION

The use of proton-beam based radiotherapy offers a number of advantages over more traditional high energy photon sources, the most significant of which being the decreased integral dose delivered to the patient while still achieving the necessary target dose. For most treatment sites, protons offer greater tumor conformality with fewer beams than with photon techniques. The unique depth-dose distribution of protons, which includes a Bragg peak after which nearly all protons lose their kinetic energy, allows clinicians to either deliver a higher dose to the tumor, increasing the probability of tumor control, or to reduce morbidity, or a combination of the two options. Proton therapy is particularly appealing for the treatment of tumors in the brain, skull base, and close to the spine, in which the target is close to a critical structure. By delivering less integral dose to surrounding tissues, the use of proton therapy reduces the side effects (healthy tissue necrosis, etc.) experienced as a result of dose delivered to healthy tissue. [Hall, 2006]

The advantages of proton beams as a source of therapeutic radiation were first realized in 1946 by Dr. Robert Wilson [Wilson, 1946]. Building off of Dr. Wilson's work, scientists in the 1960's created the first proton therapy centers by modifying particle physics research facilities. The development of hospital-based proton therapy centers began around 1990, and today 11 such centers exist throughout the world, with 15 more proposed or under construction. Although relatively esoteric compared to the ubiquity of traditional photon based radiotherapy centers, protons are a rapidly growing tool in the arsenal against cancer.

While there is much to applaud about radiation therapy there remain important problems, one of which this research seeks to address. Currently, there are no methods to predict or monitor the proton depth-dose characteristics *in situ*. As a result, the clinical advantage afforded by the sharp distal falloff in the depth dose profile of protons can not be fully exploited; an overestimate of proton path length could cause an undershoot of the beam, resulting in an incomplete tumor dosage and a decrease in tumor control probability, while an underestimate of the proton path length would cause over-dosages of healthy tissues. Uncertainties, including CT artifacts, tumor shrinkage, and setup variations, are taken into account by adding a safety margin to treatment plans, which reduces the clinical advantage of protons. An accurate method of monitoring distal

edge falloff in administered fields would help maximize dose to the target, while minimizing dose to healthy tissues distal to the tumor. In addition, precise knowledge of the distal edge falloff would allow clinicians to use gantry angles in which the proton beam points directly at a critical structure. Traditionally beam range uncertainties made such beam trajectories too risky to use on patients, but with confirmation of the beam range, range uncertainty would no longer present a problem.

One method of monitoring proton therapy delivery is by detecting the positron emitters (^{11}C and ^{15}O) created as the proton traverses the body. Coincident detection techniques used in a PET/CT scan determine the position of origin of the detected annihilation photons. However, the concentration of such positron emitters is relatively low (~1kBq/mL per Gy of absorbed dose), and combined with the short half-lives of the positron emitters and the difficulties of monitoring patients soon after treatment, there are still quite a few challenges to overcome before this becomes a viable, efficient option for monitoring dose delivery. [Parodi, 2007a&b] [Knopf, 2008]

We aim to address the problem of proton dose delivery by assessing the feasibility of measuring the gamma rays emitted during therapy via inelastic proton scattering, or a (p, p' γ) reaction, from carbon, oxygen, and nitrogen, among others. An induced prompt gamma activity from oxygen of ~3.5 MBq/mL from a 2 Gy treatment is expected - considerably larger than the PET signal. Depending on mean proton energy, proton flux, and elemental composition, the rate of emission will vary with depth in the target volume.

The impetus for interest in this technique was a study by Min et al., in which they were able to successfully characterize the depth-dose profile of the proton beam in a water tank by measuring the prompt gamma fluence at various points along the beam. [Min, 2006] Subsequent studies have begun at Massachusetts General Hospital, as well as the MD Anderson Cancer Center.

2 RADIATION THERAPY: BACKGROUND AND SIGNIFICANCE

2.1 RADIATION THEORY AND INTERACTIONS

Radiation, defined as a microscopic wave or particle which transmits energy from one medium to another, comes in a multitude of varieties, all with different sources and a unique set of physical interactions with their environment. The massless photon, for example, is produced via the acceleration of a charged particle (Bremsstrahlung, or X-rays) and the de-excitation of a nucleus (γ rays). The other commonly encountered form of neutral radiation is the neutron, a fermion ejected from excited nuclei via fission or fusion. For charged particles, we have electrons, leptons which are created from the decay of excited nuclei (β^- particles) or the absorption of photons (photoelectrons), as well as hadrons, heavy charged particles ranging from single protons to large ions, most of which are produced during fission, fusion, or ionization. [Hall, 2006] [Turner, 2004]

As one may suspect, the variation of particle sizes, masses and charges leads to a variety of interactions with matter. Photons, for example, transfer some or all of their energy to both orbital electrons and nuclei, as well as spontaneously transform into an electron/positron pair (only occurring if the photon's energy is greater than 1.022 MeV, the rest mass of the particle pair created). Electrons collide with orbital electrons and decelerate in proximity to nuclei, while neutrons collide with nuclei. Hadrons experience a variety of interactions with matter, mostly colliding with orbital electrons, but they also collide with nuclei, both taking valence orbital electrons from the atom and fissioning (in the case of heavy ions) as they traverse matter. [Turner, 2004]

The variety of interactions that cause a particle to lose its kinetic energy result in different transmission characteristics among the various flavors of particles. Photons, for example, experience an evanescent (with respect to material thickness) transmission:

$$I = I_o B(E) e^{-\int \mu(E) x dE} \tag{2.1}$$

where I is the beam intensity detected at the distal end of the beam in a material, I_o is the initial intensity of the beam (or intensity of the beam at the proximal edge of the beam in a material),

$B(E)$ is the buildup factor, μ is the attenuation coefficient, E is the photon energy, and x is the material thickness. [Turner, 2004]

In contrast, protons exhibit a more complicated energy loss profile which must take into account the ionization potential of the colliding electrons, the relativistic speed of the proton, and the electron density of the target, all of which is taken into account with the Bethe Bloch formula:

$$-\frac{dE}{dx} = \frac{4\pi}{m_e c^2}\rho\frac{Z}{A}\frac{z_p^2}{\beta^2}\left[\ln\left(\frac{2m_e\beta^2c^2T_{\max}}{I^2(1-\beta^2)}\right) - 2\beta^2 - \delta\right] \quad \textbf{(2.2)}$$

Where $\rho\frac{Z}{A}$ is the electron density of the target, z_p is the charge of the proton, $\beta = \frac{v}{c}$, and I is the ionization potential of the target. [Turner, 2004] Ultimately, this formula yields a transmission in which the majority of the protons pass through a given thickness of material, experience a Bragg peak (a peak of dose deposition) after which nearly all protons lose their kinetic energy. (Figure 2-1)

Figure 2-1: MCNPX simulation of a 150 MeV proton beam entering and stopping in a Lucite phantom. Beam enters at bottom of figure and traverses 15cm of Lucite before stopping. Note the beam broadening as the protons traverse the phantom and the distinct range of the beam. Each blue dot represents one collision between a proton and the phantom material – as the proton beam traverses more material and loses more energy, the density of collisions per unit length increases, demonstrating the higher linear energy transfer (LET) of proton beams at the Bragg peak.

Ionization and excitation of atoms are the primary means of energy loss for a high energy proton traversing matter, with nuclear collisions becoming the more prevalent interaction as the proton loses energy. As demonstrated by

$$Q_{Max} = \frac{4Mm}{(M+m)^2} E \tag{2.3}$$

where $\mathbf{Q_{Max}}$ is the maximum energy transfer between particles for an elastic collision, **M** and **m** are the masses of the particles, and **E** is the energy of the incoming particle, the proton is only able to transfer a small amount of energy to each electron with which it collides, yielding the relatively straight paths observed in Figure 2-1.* If enough energy is supplied to the electron for it to escape its atomic orbit, the electron becomes a δ ray. Occasionally a proton will undergo elastic scattering with a nucleus (as Rutherford observed with alpha particles), yielding a substantial deflection from the proton's original trajectory, although this has an extremely low probability. [Turner, 2004]

Inelastic scattering with nuclei is another possibility, and it causes the effects we aim to study. During an inelastic collision, some of the energy imparted by the proton is absorbed by the incident nucleus, with two likely possibilities. The first is that it knocks off a nucleon, say a neutron, yielding a (p, p' n) reaction. The second possibility is that sufficient energy is not imparted to knock off a nucleon, and instead a nucleon(s) is raised to a higher energy level. Both possibilities create an unstable nucleus – the first restabilizes via β^+ decay, the second via γ decay (which also competes with electron capture). [Turner, 2004]

2.2 RADIATION BIOLOGY

The variation in particle interactions inherently leads to a variety of biological effects as radiation traverses an organism. For simplicity, we will only consider the effects to a cell's DNA, which can be categorized as either direct effects, those which directly cleave one of more DNA strands, and indirect effects, those which create reactive species (ie, H_2O derived free radicals such as HO•, the hydroxyl radical), which virulently attack DNA and other surrounding molecules in the cell

* The mass of a proton more massive than an electron by a factor of 1836, which yields a maximum energy transfer of 0.218% E.

nucleus. Free radicals are created with some frequency during natural cell processes (most notably, the TCA cycle and ATP synthesis, a series of chemical reactions undertaken by all aerobic organisms in order to produce usable forms of metabolic energy), and the body is equipped with free radical scavengers to handle their presence (Vitamin E, among others). [Voet, 1995] If a free radical isn't scavenged, its attack on DNA may be reversed by the presence of an SH compound, which will chemically absorb the radical. The presence of O_2, however, increases the susceptibility of a cell to indirect DNA attacks by binding with the free radical after it has attacked the DNA; this peroxide radical can no longer be absorbed by an SH group, thus making permanent the damage done to the DNA. As a result, hypoxic cells are less susceptible to the indirect effects of radiation, while cells with a high concentration of O_2 are more susceptible. Photons and electrons, having little or no mass, primarily produce indirect effects, while hadrons produce both indirect effects (creating δ particles) and direct effects via collisions with nuclei in DNA, breaking bonds and cleaving DNA strands. [Hall, 2006]

Given that indirect effects are more easily repaired than direct effects, indirect effects are less biologically damaging per particle. As a result 1 Gray (1Gy=1J/kg deposited by radiation) of photon radiation has a lower tissue lethality than 1Gy of hadrons, and the relative biological effectiveness of hadrons, defined as the ratio of photon dose to test radiation dose to produce a given biological endpoint, is approximately 1.1. [Hall, 2006] As a result, a conversion of photon dose to proton equivalency, designated as Gy[RBE] (formerly known as GyE) is required for treatment planning. [ICRU, 2008]

Not all cells are equally susceptible to radiation, nor do they all repair damage equally. Healthy cells, on average, are better able to repair radiation damage than cancerous cells which have a higher metabolic rate. As a result of this, and in attempting to reoxygenate the hypoxic regions found in large tumor masses, treatments are typically performed in 20-30 fractions over 4-6 weeks. This allows the healthy cells to repair between fractions, and it allows the less susceptible hypoxic cells acquire the vasculature once belonging to the outer, now necrotic, cancerous cells, resulting in a more susceptible tumor core for the next treatment fraction.* [Hall, 2006]

* Note that cancer cells will also repair between fractions, but their repair mechanisms are often slower than those of healthy cells.

2.3 RADIATION THERAPY

The most prevalent form of radiation therapy involves the use of high energy X-rays. Photons were the first radiation artificially produced (X-rays), their physics is well known, and the required accelerators are relatively inexpensive to produce. Their abundance has caused all radiation oncology training to focus on photon therapy, resulting in a significant library of literature on treatment options and outcomes for various cancers. [Hall, 2006]

Photons do present some distinct limitations on efficacy and tissue sparing. As discussed above, they primarily produce indirect effects to a cell's DNA. This, however, can be overcome by overdosing a tumor volume; a sufficient dose will kill any cell regardless of susceptibility, and a wealth of information exists on how much dose is required to kill a particular tissue type.

More limiting is the depth dose profile of a photon beam in tissue. As photons deposit energy in tissue, maximum dose is delivered to the entry tissue, with an evanescent dose being delivered to all tissues below the surface. As a result, all tissues are bathed in a dose, potentially severely damaging healthy tissue. (Figure 2-2) This is not to say that photons can not be used to safely treat tumor sites; current 3-D conformal and Intensity Modulated Radio-Therapy (IMRT) techniques make use of multiple gantry angles and beam directions in order to keep the integral dose relatively low to any given portion of healthy tissue while obtaining the required tumor dose.

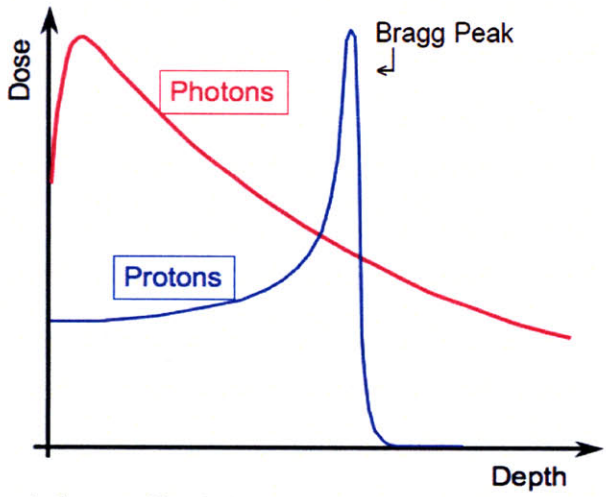

Figure 2-2: Depth dose profile of photons and protons in tissue [Bortfeld, HST.187]

Protons, however, posses a completely different, discrete dose profile, with a plateau and a 'Bragg peak' of dose after which the proton beam stops, depositing no more energy in the tissue. As a result, much greater tumor conformation with fewer beams, as well as greater healthy tissue sparing can be achieved, resulting in more dose safely being delivered to the tumor while sparing healthy tissue from lethal doses of radiation. Tumors of all types can be treated with protons and the beam penumbra is smaller than photon penumbra for depths shallower than approximately 15cm. [Turner, 2006] [Bortfeld, HST.187] Because hadrons cause also direct radiation effects, they are also more effective at treating tumors with a hypoxic core, as radical scavengers are unable to assuage the damage done by their direct radiation effects.

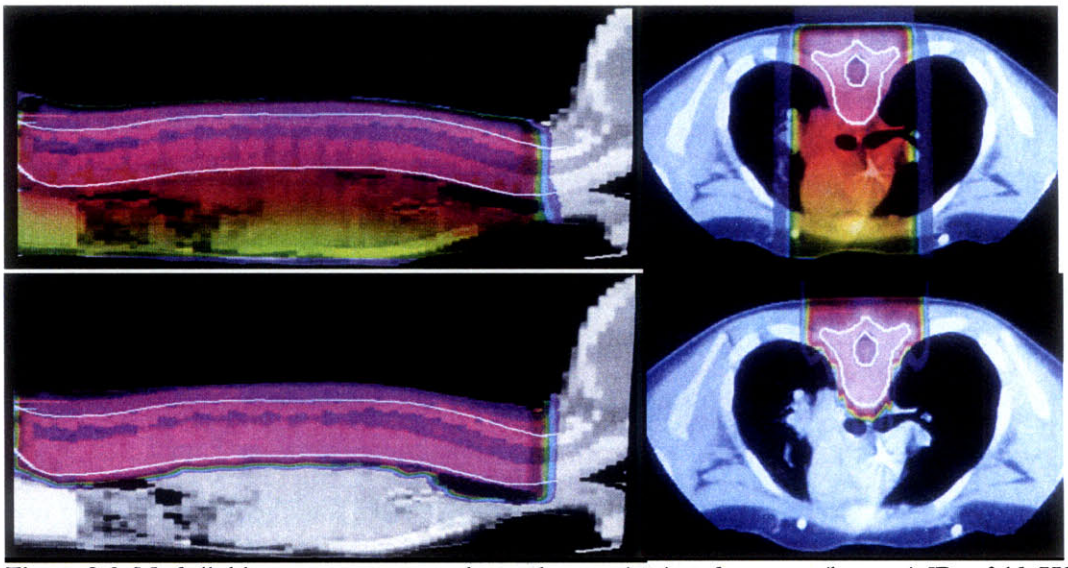

Figure 2-3: Medulloblastoma treatment plans: photons (top) and protons (bottom) [Bortfeld, HST.187]

As can be seen in Figure 2-3, the photon treatment bathes a large percentage of the abdominal cavity in doses exceeding 60% prescribed dose (red), while the proton treatment confines the radiation dose to the treatment volume, resulting in lower morbidity due to the significantly lower dose deposited in the tissues in the abdominal cavity. [Turner, 2006]

2.4 BRAGG PEAK: BOTH A BLESSING AND A CURSE

Proton therapy requires precise application in order to exploit its therapeutic advantage over photons. If a situation arises in which the healthy tissue is inadvertently exposed to the Bragg

peak, healthy cell mutation and radiation induced necrosis and scar tissue may result. This is a relative non-issue for photon therapy, where a 1cm lateral deviation results in a change of a few per cent in dose deposition (~3% with a 6MV X-ray beam). [Gierga, 2009] In proton therapy, however, the same 1cm lateral deviation may result in a 100% change in dosage, potentially completely undershooting the target volume and depositing all dose in healthy tissue. [Hall, 2006] [Turner, 2004] Two potential sources of this error are relatively easily corrected; physiologic movement such as that of the lung or the heart (4-D treatment planning) and patient misalignment (physically implanted markers and X-ray guided landmark alignment are used prior to each fraction).

There are various sources of dose delivery error for which current techniques can not completely compensate. CT 'star' artifacts, caused by fillings or other high-Z materials in the patient, lead to an inaccurate calculation of tissue density, which is used directly by treatment planning algorithms to determine the proton energies required for a specific depth penetration in tissue. If the computed tissue density is higher than the actual value a higher proton energy will be selected by the planning software, resulting in an overshoot of the proton beam. Therefore, dosimetrists usually overwrite artifacts in CT images using estimated tissue densities, but this is an imperfect process.

Another source of error is tumor shrinkage. Depending on the type of tumor, the volume may decrease significantly over the course of treatment. (Figure 2-4) As healthy tissue moves into the volume previously occupied by tumor, healthy tissue is exposed to the Bragg peak during treatment. While one possible remedy may be to CT the patient intermittently during treatment, the time and man power required to compare CT images and reevaluate treatment plans multiple times during treatment is unrealistic. The number of patients that would benefit from such work and increased radiation exposure is relatively small (because few tumors shrink to the degree that there is significant overdosing of healthy tissues) compared to the number of patients receiving proton therapy. [Mori, 2007]

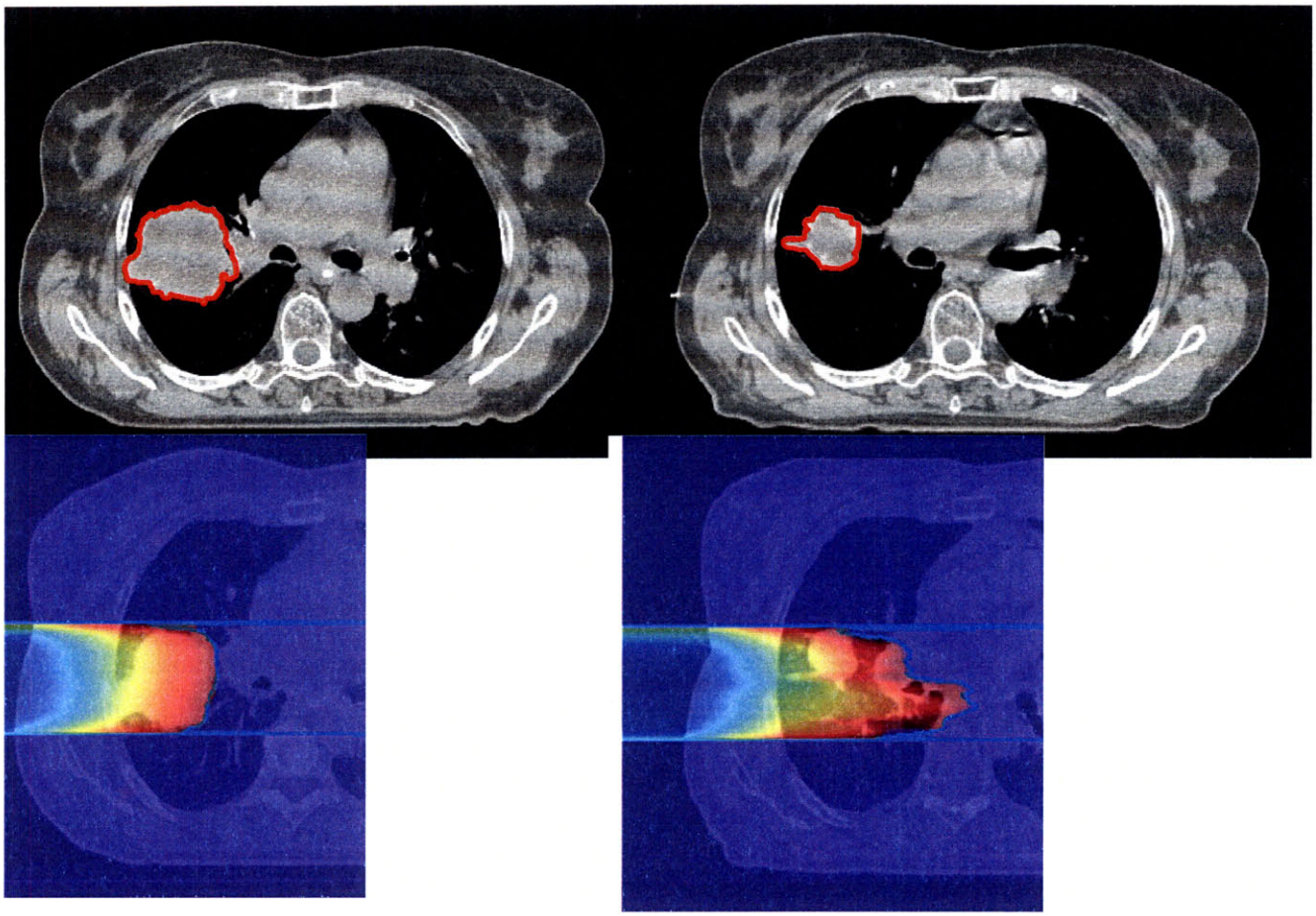

Figure 2-4: Lung tumor CT (top) and proton treatment plan (bottom): initial scan, gross tumor volume (GTV) 115cc (left), 5 weeks into treatment, GTV 39cc (right). Tumor volume hilighted in red. [Mori, 2007]

Yet another source of error that is frequently encountered in radiation therapy is patient movement during treatment. The most extreme cases are encountered in thoracic cases (lung, heart, etc.) However, new treatment planning methods and *in situ* monitoring devices (4D treatment) have reduced the error associated with such movements. Patient movement from treatment to treatment, which results from inconsistent patient positioning is more of a problem. While this if often compensated for by using implanted seeds or pre-treatment X-rays, which use landmarks for proper alignment, the methods are imperfect and misalignments can happen, as demonstrated in Figure 2-5.

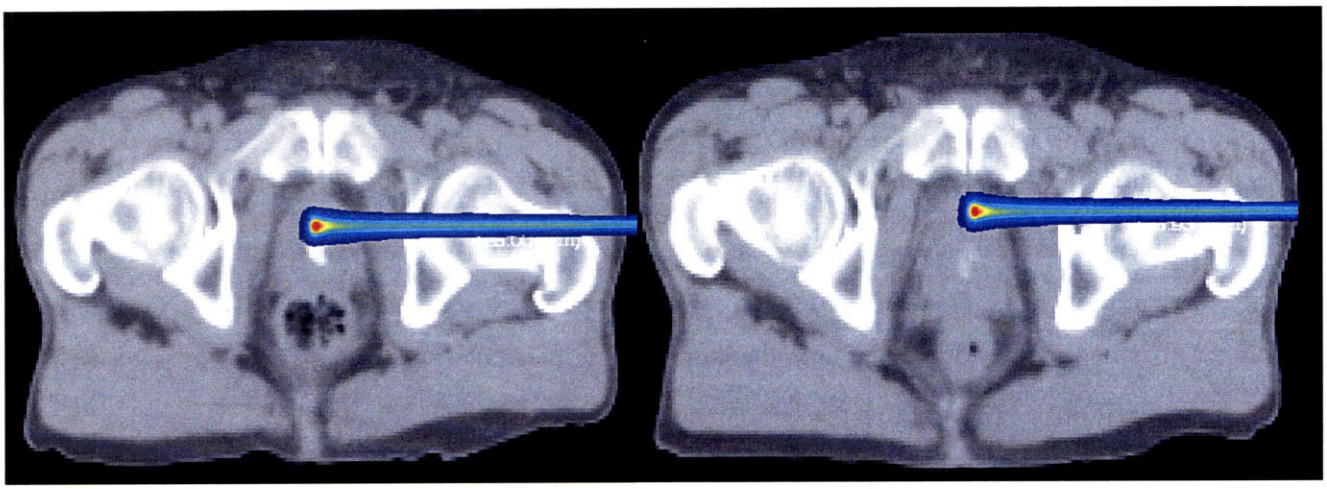

Figure 2-5: Prostate Treatment CT 08 Jan 2000 (left) and 11 Jan 2000 (right). Note the rotation of the femoral head and the increased bone traversal length of the beam for 11 Jan. [Chen, 2000]

With such significant sources of error, it is difficult to ensure that the Bragg peak, which has saved thousands of patients' lives and quality of life, does not inadvertently kill healthy tissue in a few patients. Clinicians conservatively add a margin to the tumor volume to account for such uncertainties – this both decreases the potential risk to the patient and reduces the advantages of using a proton beam over more traditional high energy X-rays A quick, reliable and safe means of imaging to ensure that the Bragg peak is being isolated solely to the tumor volume would greatly help to ensure that treatments are being delivered as prescribed and maximize the potential benefits afforded by proton physics.

2.5 CURRENT METHODS FOR *IN VIVO* PROTON THERAPY MONITORING

2.5.1 POSITRON EMISSION TOMOGRAPHY

Positron Emission Tomography, or PET, has been around for decades and is a staple of the nuclear medicine branch of diagnostic radiology. Antimatter, colloquially thought of as the stuff of science fiction, provides the physical backbone of PET imaging. Positrons are created by proton rich nuclei, which convert a proton (p^+) into a positron (β^+), neutron (n^o), and a neutrino (ν), plus kinetic energy for the neutrino and the positron.

$$p^+ \rightarrow \beta^+ + n^o + \nu \tag{2.4}$$

This positron annihilates when in contact with an electron. Two annihilation photons result, each with an energy of 511keV traveling antiparallel to each other. These photons which are detected during PET imaging. [Turner, 2004]

For nuclear medicine applications, a positron emitter is attached to a tracer molecule. Most commonly, ^{18}F is attached to glucose, resulting in florodeoxyglucose (FDG). Cancers, often having a higher metabolic rate than surrounding healthy tissue, have a higher uptake of glucose, which results in a brighter PET signal in the tumor volume. [Cho, 1993]

Once the FDG is injected and allowed to distribute throughout the body, the patient is placed in a ring of photon detectors (scintillating crystals attached to photomultiplier tubes) which detect the annihilation photons. [Knoll, 2000] Coincident detection techniques and reconstruction algorithms are used to determine the origin of each photon pair; higher photon fluence originating from a particular voxel indicates higher positron emitter concentration. [Cho, 1993]

Positron emitters are also created during proton therapy. As the proton traverses tissue, it mainly loses energy via collisions with orbital electrons, knocking the electrons out of orbit and creating δ-rays. Less frequently, a proton will collide with a nucleus, which may lead to a multitude of events; if the proton is of sufficiently low energy it may be absorbed or it may scatter, taking with it an orbital electron and becoming a hydrogen atom. Occasionally, upon collision with a nucleus, the proton will knock off a neutron. If this happens to occur in carbon or oxygen (two commonplace elements in the body) ^{15}O and ^{11}C will result, both of which are proton rich, unstable nuclei that undergo positron decay with halflives of approximately 2 minutes and 20 minutes, respectively. (Figure 2-6) The positrons created from these two isotopes behave identically to the positrons used for PET imaging. As a result, it is possible to use a standard PET scanning device to measure the concentration of ^{15}O and ^{11}C in a particular volume. [Parodi, 2007b]

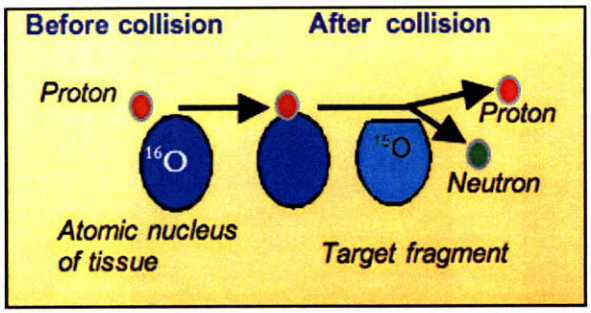

Figure 2-6: Schematic of ^{15}O production [Bortfeld, 2008]

There lies a correlation between the energy deposited per mass of tissue and the number of positron emitters created; the PET signal is proportional to the proton fluence and the probability of a proton-nucleus interaction which results in a positron emitter. [Parodi, 2007a] Most importantly, the distal fall-off of the PET signal as a function of depth correlates approximately with the dosimetric distal fall-off of the beam. The PET scan is completed immediately after treatment, providing clinicians with immediate feedback as to the efficacy of the treatment and the deposition of dose by the proton beam. (Figure 2-7)

However, PET verification is not without its drawbacks. The short halflives of the ^{15}O and ^{11}C require scanning immediately after treatment. After 20 minutes, the ^{15}O signal is essentially zero, and the ^{11}C signal has been reduced by a factor of 2. Biological factors affect the signal decay as well – vasculature sweeps activated atoms away from their original irradiation site, ultimately reducing the half life signal and decreasing the signal to noise ratio obtained from scanning. [Parodi, 2007a]

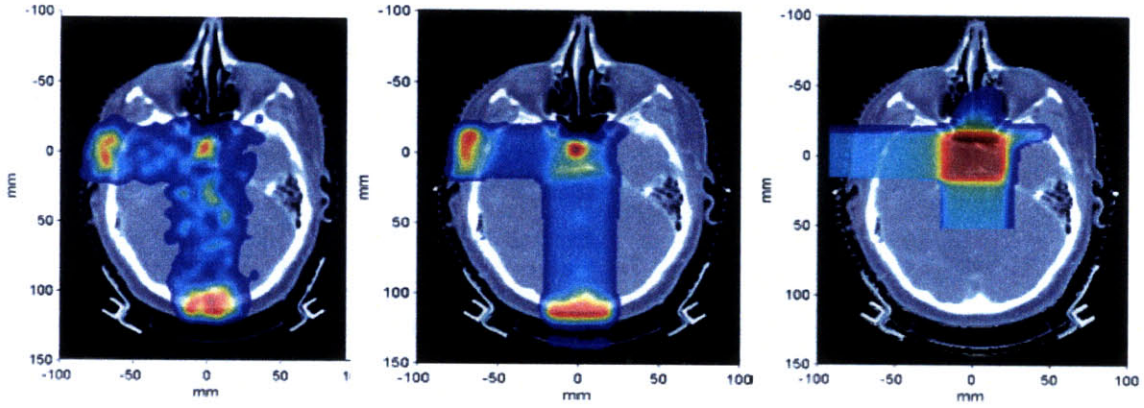

Figure 2-7: Measured PET (left) Monte Carlo PET (middle) and treatment plan dose (right) for a patient with pituitary adenoma receiving two orthogonal fields. [Parodi, 2007b]

The human body is not homogeneous. Tissues have varying composition, and different tissues emit different signal intensities when subjected to the same dose. While this in and of itself is relatively easily compensated for, when taken in conjunction with the biological decay and short-lived isotopes upon which the technique relies, it is difficult to obtain a high SNR image that accurately reproduces the dose profile in the patient. [Parodi, 2007a] The inability to provide a 1:1 correlation between the PET signal and dose has caused most current studies to use PET as a range verification tool, instead of using it to recreate the dose profile, with clinically acceptable levels of uncertainty. [Parodi, 2007b]

2.5.2 Post Treatment Irradiation MRI of Vertebral Discs

Recent studies have shown that spinal proton treatment causes a characteristic pattern of fatty conversion in the vertebral bone marrow that is visible on post treatment MRI scans. [Krejcarek, 2007] Groups have shown that a T1-weighted hyperintensity of bone marrow from fatty conversion is detectable by the end of radiation treatment and persists for at least 11 months.(Figure 2-8) [Blomlie, 1995] [Cavenagh, 1995] Promising work is being conducted in developing a dose to post-treatment MRI signal intensity curve.

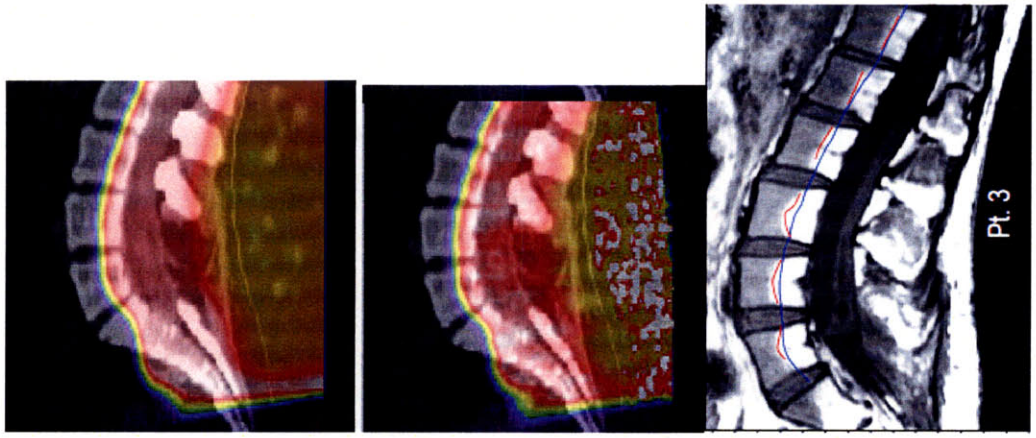

Figure 2-8: Treatment plan (left) Monte Carlo calculation (middle) and MRI (right, blue line is planned 50% isodose line, red line is estimated true 50% isodose line) of lower Lumbar

While the results are promising, the main drawback of this method is the timescale involved. Current studies indicate that the observed T1 hyperintensity initially occurs after treatment. As a result, the clinician can not use this information to adjust the patient's treatment. While the information provided is useful for quality assurance and future treatment planning practices purposes, the damage has already been done to the patient at hand by the time the effect is visible.

2.6 *IN SITU* PROTON RANGE VERIFICATION ASSESSMENT VIA PROMPT GAMMA DETECTION

While the aforementioned PET and MR methods have yielded some promising results and warrant further research, they have inherent flaws and complications. The effect that biological decay has on the PET signal makes it is difficult to obtain a high SNR representation of the beam range with the PET method. And, while the MRI method provides wonderful data in hindsight, it yields no data in the timeframe necessary for a clinician to change a patient's current treatment plan.

Prompt gamma emission detection has the potential to provide meaningful proton range verification *in situ* while avoiding some of the pitfalls discussed with other techniques. The technique has the potential to provide instant data to the clinician during treatment, meaning that the data can be analyzed by a clinician after any given fraction, and the remaining fractions can be

adjusted if needed. But information can potentially be gained regarding treatment before the first fraction is delivered. The high gamma emission rate of approximately 3.5 MBq/mL/Gy, considerably larger than the PET isotope production rate, may allow clinicians to deliver a micro-fraction, which would mimic the actual treatment fractions while delivering a small dose to the patient. This would allow clinicians to monitor the range and ensure compliance with the treatment plan of the treatment beam before even one fraction was delivered to the patient. While the data may not be as striking and vivid as the images produced via PET/CT and MRI, the data are no less useful, and it is this simplicity and the high potential SNR offered by the high activity rate that make prompt gamma emission detection such a potentially powerful tool.

3 PROMPT GAMMA: BACKGROUND AND INITIAL EXPERIMENTS

3.1 GAMMA DECAY

Gamma emission occurs when a nucleus decays from an excited state to a lower or ground state and emits a photon of energy equal to the difference between the two nuclear states, and is analogous to the emission of characteristic X-rays. [Krane, 1988] In the case of proton therapy, the excited nuclear state results from inelastic scatter between the proton of energy E_p and a nucleus in the material through which the proton is traversing. The proton collides inelastically with the nucleus, scattering with an energy E_p', imparting an energy to the nucleus $E_{nucleus}=E_p-E_p'$. This excess energy in the nucleus causes one or more nucleons to enter an excited state. When the(se) excited nucleon(s) return to their ground state, they emit a gamma with energy $E_\gamma=E_{nucleus}$. This reaction can be described in shorthand as A(p, p' γ)A. For example, one reaction that occurs with carbon is $^{12}C(p, p' \gamma^{4.44MeV})^{12}C$, or

$$p+{}^{12}C \rightarrow p'+ {}^{12*}C$$
$${}^{12*}C \rightarrow {}^{12}C + \gamma_{4.44\,MeV}$$

Given that nuclei have quantized energy states, such gamma emissions are quantized and particular energies are characteristic of a given nucleus. Table 3-1 describes some of these characteristic gamma rays, and Table 3-2 shows the composition of brain, muscle, water, and polymethyl methacrylate (the latter two being common phantom materials).

Table 3-1: Summary of proton nuclear interactions with the elemental constituents of tissue [Dyer, 1981] [Kiener, 1998]

Isotope	Reactions	Gamma-ray Energies (MeV)
^{12}C	$^{12}C(p, p' \gamma)^{12}C$ $^{12}C(p,2p \gamma)^{11}B$	4.44
^{14}N	$^{14}N(p, p' \gamma)^{14}N$	1.64, 2.31, 5.11
^{16}O	$^{16}O(p, p' \gamma)^{16}O$	2.74, 6.13, 6.92, 7.12

Table 3-2: Elemental composition (atom fraction) and density of brain, muscle, and representative phantom materials. [ICRU, 1989]

	Density	Elemental Atom Fraction			
	($g\ cm^{-3}$)	H	C	N	O
Brain	1.040	0.646	0.074	0.009	0.271
Muscle	1.014	0.633	0.074	0.015	0.278
Water	1.00	0.667	-	-	0.333
PMMA	1.19	0.533	0.333	-	0.133

The probabilities of such reactions depend on the energy of the incident proton. The cross section of ^{16}O, for example, has a threshold of 8-10MeV, and a maximum of approximately 0.2 barns. (Figure 3-1)The cross section of ^{16}O is representative of the other reactions listed in Table 3-1.

A typical proton therapy plan administers the proton beam at a rate of approximately 2Gy/min, or $2.1x10^{14}eV/cm^3/g$. Dividing by the proton stopping power of approximately $40MeV/cm^2/g$ yields a nominal proton flux of $5.3x10^9/cm^2/s$. The inelastic emission rate per unit volume can be estimated as the product of the flux times the cross section ($0.2x10^{-24}cm^2$) times the number density of the particular nucleus (in this case, ^{16}O, $3.34x10^{22}/cm^3$). This results in a gamma emission rate of approximately 3.5 MBq/mL. As tissue composition changes and proton energy decreases along the proton beam path, the rate of emission will vary with depth in target and the emission fluence peak will be slightly proximal to or at the Bragg peak (depending on the initial beam energy), as suggested by the cross section curve in Figure 3-1.

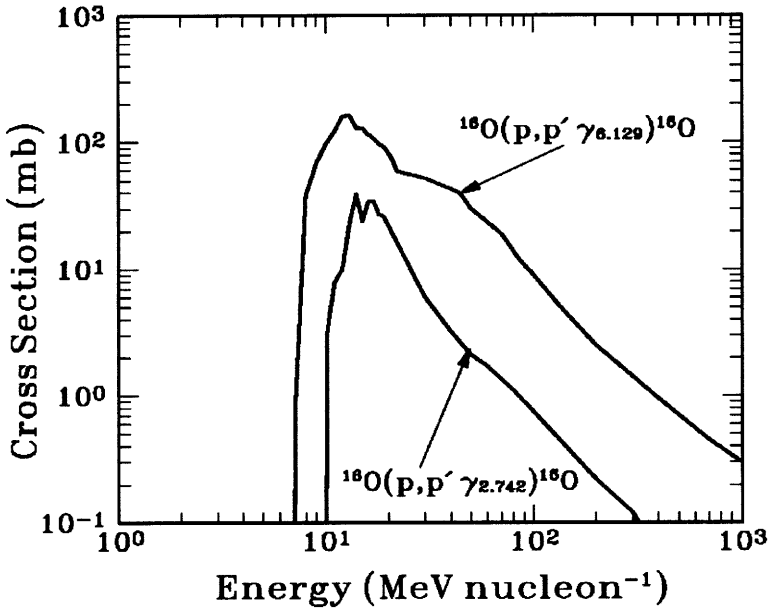

Figure 3-1: Proton inelastic scattering cross section for two different characteristic gamma ray lines (6.13MeV and 2.74MeV) [Kiener, 1998]

3.2 INITIAL KOREAN STUDY

The first study conducted at the National Cancer Center of Korea by Chul-Hee Min *et al.* used a 100-200MeV proton pencil beam incident upon a water phantom. [Min, 2006] A CsI(T1) scintillator was used to detect the gammas, and was collimated such that only gammas emitted orthogonal to the central axis of the proton beam were registered. The collimator consisted of two parts: a paraffin layer and a lead and B_4C layer. The paraffin layer shielded the scintillator from the high energy spallation neutrons emitted during therapy (which are mostly forward oriented, but strong enough to compete with the photon signal at 90°). This paraffin layer moderated the neutrons, the B_4C in the lead captured the neutrons by the $B(n,\gamma)$ reaction, and the lead blocked these unwanted gammas. The lead layer also shielded from gammas that are not emitted at 90° and would otherwise taint the signal. (Figure 3-2)

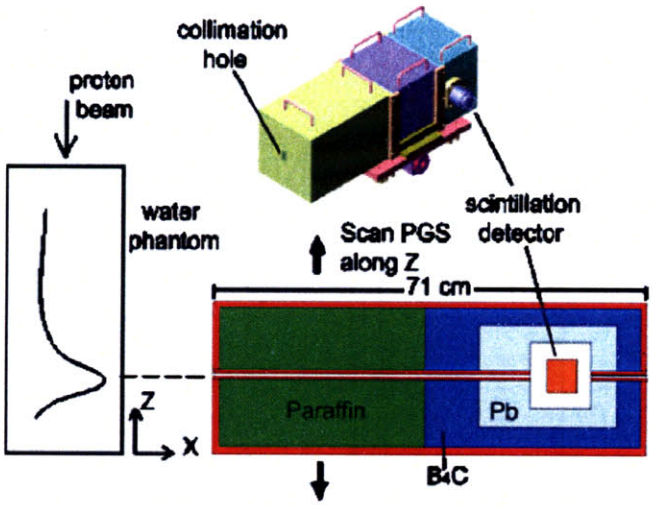

Figure 3-2: Isometric and sectional views of the collimator setup [Min, 2006]

The prompt gamma emission rate correlated strongly with the proton depth dose profile, with a gamma emission peak approximately at the location of the Bragg peak. (Figure 3-3) A significant signal was observed in the plateau region, and the gamma signal dissipated distal to the Bragg peak.

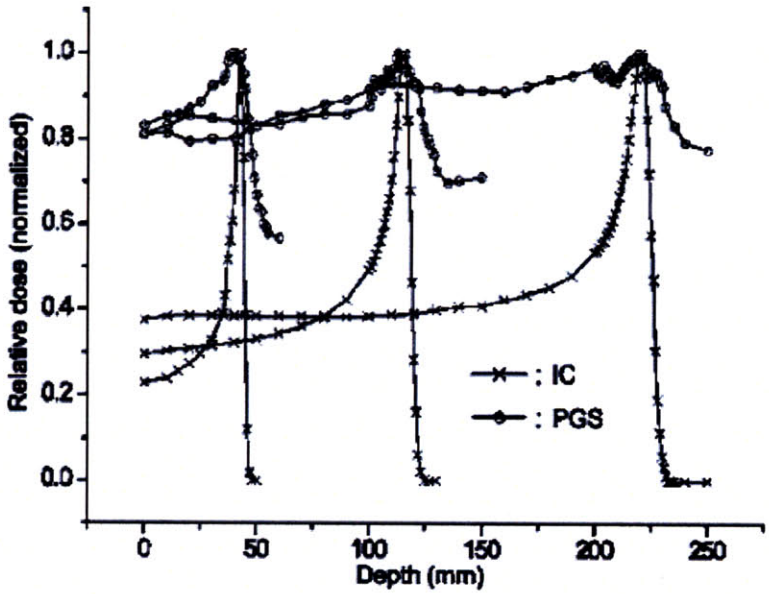

Figure 3-3: Comparisons of the depth-dose distributions measured by the ionization chamber (for proton dose profile) and the prompt gamma scanner measurement at E_p=100, 150, and 200MeV. Note the slight dip in photon signal slightly proximal to the Bragg peak. [Min, 2006]

3.3 PRELIMINARY EXPERIMENTS AT MGH

Initial experiments were performed in one of three available therapy rooms at the Francis H. Burr Proton Therapy Center at the Massachusetts General Hospital. In order to minimize the high levels of background radiation that would normally be produced in the treatment room in beam scattering devices used during therapy, measurements were performed using a pencil beam (approximate diameter 5-6mm) with an energy of 150MeV and a beam intensity of 5nA. The beam was incident upon a cylindrical Lucite quality assurance (QA) phantom with a diameter of 10.2cm and a length of 30cm. Gamma rays were measured at 90° to the central axis of the incident beam using a cylindrical 2.5x5cm (diameter x length) NaI scintillator which was coupled to a photomultiplier tube. The detector was collimated with lead bricks, with a wall 10 cm thick and 80cm long, with a slit opening 5mm wide for the detector to view the emitted radiation. (Figure 3-4)

Pulse height data were acquired on a commercial multi-channel analyzer (Canberra industries DSA 1000) and were calibrated using the Compton peaks at 1173 and 1332 keV produced by a ^{60}Co test source. The detector was positioned 52cm from the central axis of the proton beam and was not shielded from room return scatter or radiation produced upstream in the beam line. The assembly was scanned through the depth of the Bragg peak parallel to the beam direction. A spectrum was acquired at each position for 100 MU of beam dose recorded by the dose monitoring system routinely used during therapy. A monitor unit (MU) is defined as a certain amount of charge collected in an ionization chamber and is a measure of the delivered dose in radiation therapy.

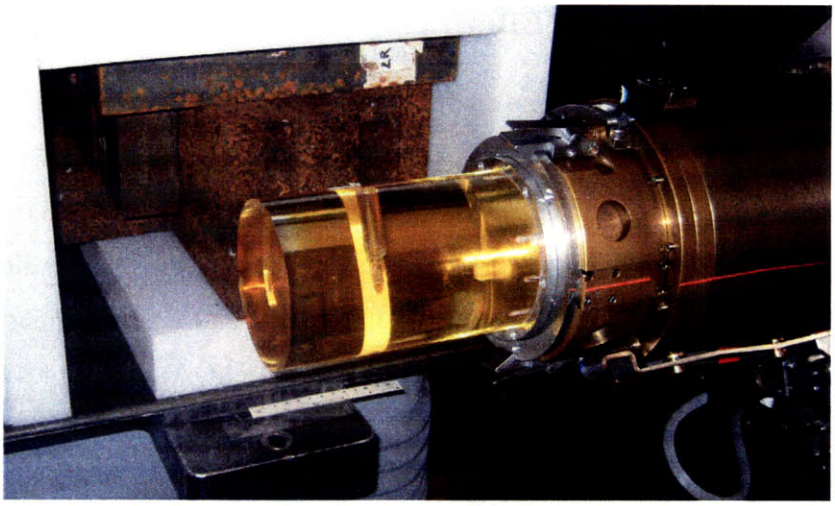

Figure 3-4: Photograph of measurement setup. NaI scintillator positioned orthogonal to the beamline behind shielding with a 5mm slit aperture (top), scanned along the beam path. Proton beam enters from the right of the image into Lucite phantom (yellow cylinder).

The measured spectrum yielded a gamma emission peak approximately 15mm proximal to the Bragg Peak, with a relatively large gamma count distal to the Bragg Peak. The gammas distal to the Bragg peak are attributed to recoil nuclei and neutrons causing activation beyond the proton beam range. The local minima at approximately 18mm proximal to the Bragg Peak is still unexplained (Figure 3-5), although a similar result was obtained by Min *et al* in the 225mm range proton beam shown in Figure 3-3.

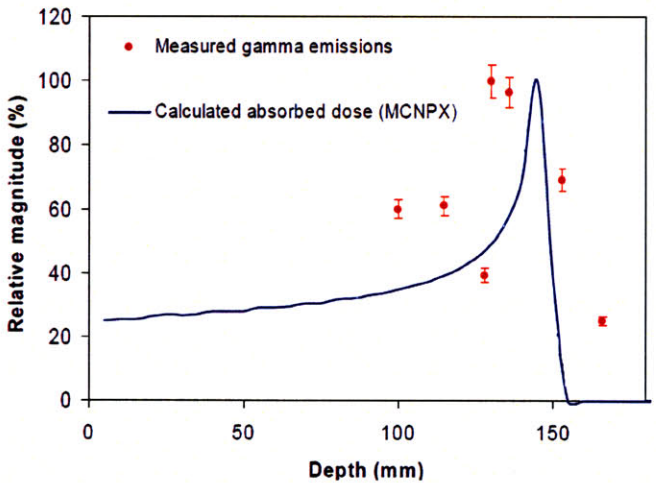

Figure 3-5: Gamma emissions measured by Kent Riley and Peter Binns as a function of distance along a Lucite cylinder for an incident 150MeV proton pencil beam plotted with the calculated proton depth dose profile.

4 EXPERIMENTAL SIMULATION: GEANT VS MCNPX

4.1 GEANT 4.8.0

Initial simulations of the MGH experiment described in Section 3.3 were run using the GEANT 4.8.0 radiation transport code developed at CERN. GEANT was chosen because it is the most ubiquitous radiation transport code used by medical physicists in the radiation oncology department at MGH. As a result, a full setup of the proton beam treatment head has been developed and benchmarked in GEANT, and Monte Carlo treatment planning for proton therapy using GEANT is being developed. [Paganetti, 2008]. Initial runs consisted of the full treatment head and Lucite phantom as well as the collimated NaI scintillator (Figure 4-1). Particle-by-particle tracking was conducted on gammas created in the phantom, as well as those that reached the NaI scintillator.

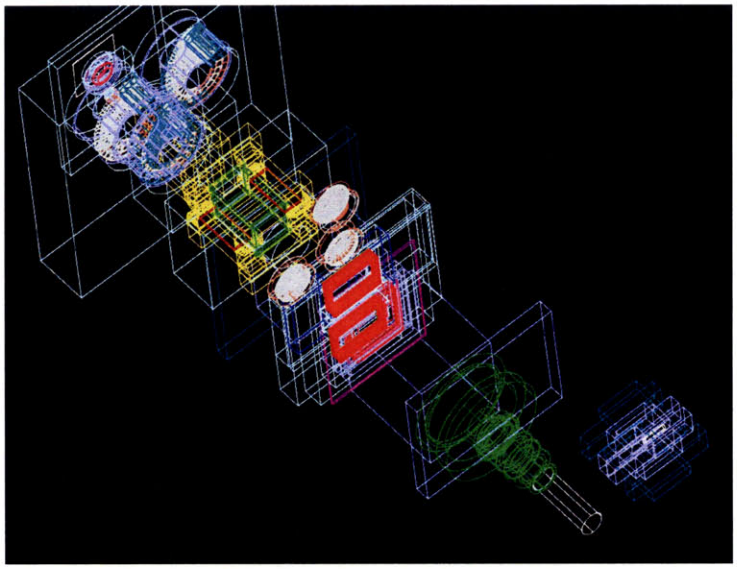

Figure 4-1: Schematic of experimental simulation. Lucite phantom visible as white wireframe cylinder in the lower right. Collimating blocks visible as purple and green wireframe boxes in the lower right. Upstream proton therapy head components (beam degrader, etc.) visible in the upper left.

However, initial simulations provided mixed results. The tally of gammas exiting the phantom yielded the characteristic gammas of the materials comprising the phantom, as expected. (Figure 4-2)

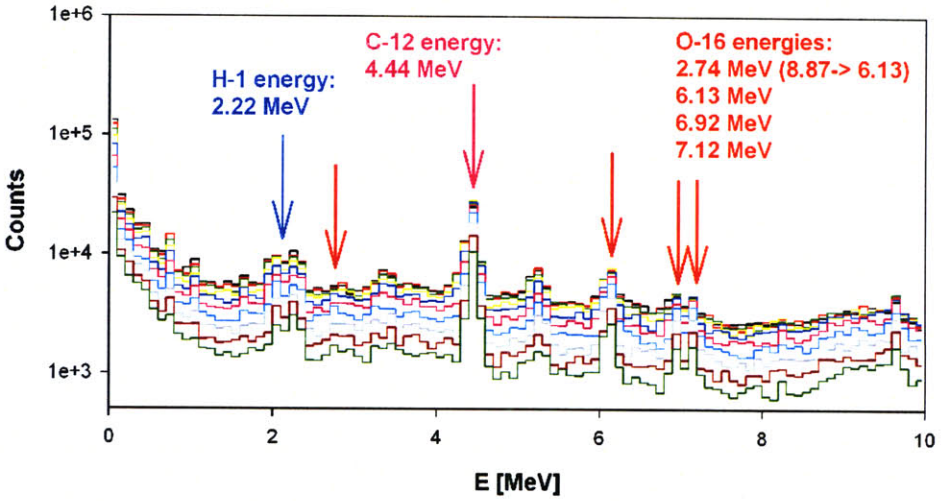

Figure 4-2: Spectrum of gammas leaving the Lucite phantom as calculated by GEANT - Gamma peaks of H, C, and O highlighted.

The gamma emission profile did not correlate with the proton depth dose profile as had the previous MGH and Korean experiments. Even when energy gating was conducted to examine only characteristic peaks, there was little distinction between the emission profile at and around the Bragg peak and the plateau region of the proton depth dose profile. (Figure 4-3)

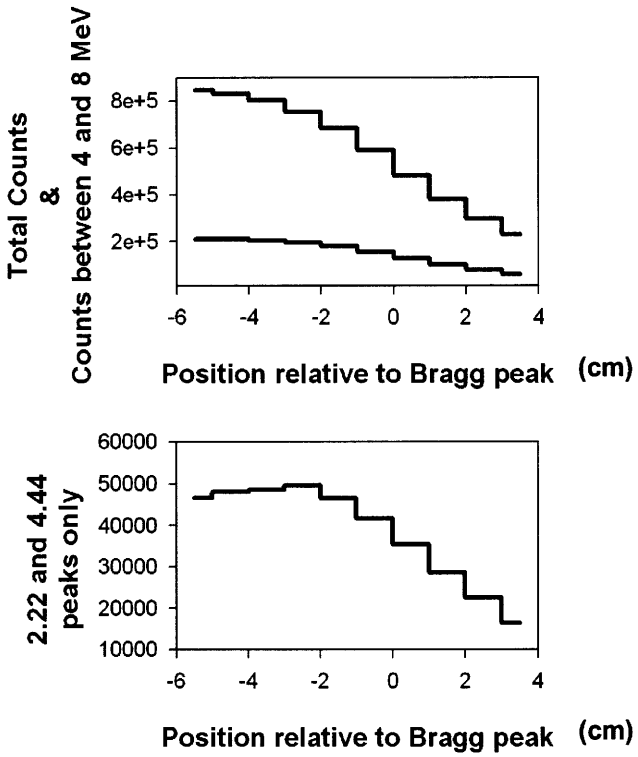

Figure 4-3: Gamma emission profile plotted relative to the Bragg Peak position

A potential cause of this unexpected gamma emission profile was the angular distribution of the emitted gammas. The angular distribution of emitted gammas from a proton beam incident on a phantom (dictated by the angular differential cross section, $d\sigma/d\Omega$) should be relatively isotropic (indicating that this is an $\ell=0$, or S-wave dominated reaction) or have a minima about 90°. (Figure 4-4) [Kiener, 1998]

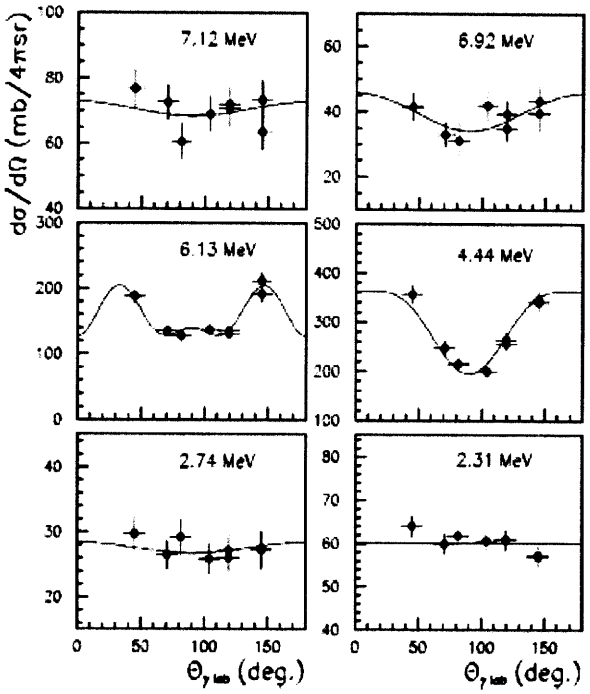

Figure 4-4: Gamma emission angular distribution for E_p=14MeV (the average energy of a proton in the Bragg peak of a 140 MeV beam) on collodion ($C_{12}H_{16}N_4O_{18}$) foils. [Kiener, 1998]

In contrast to this expected angular distribution, the gamma angular distribution varied wildly over the proton beam path, with forward directed gammas at the Bragg peak, backward directed gammas at the entrance region, and a relatively flat angular distribution in the proton plateau region. (Figure 4-5)

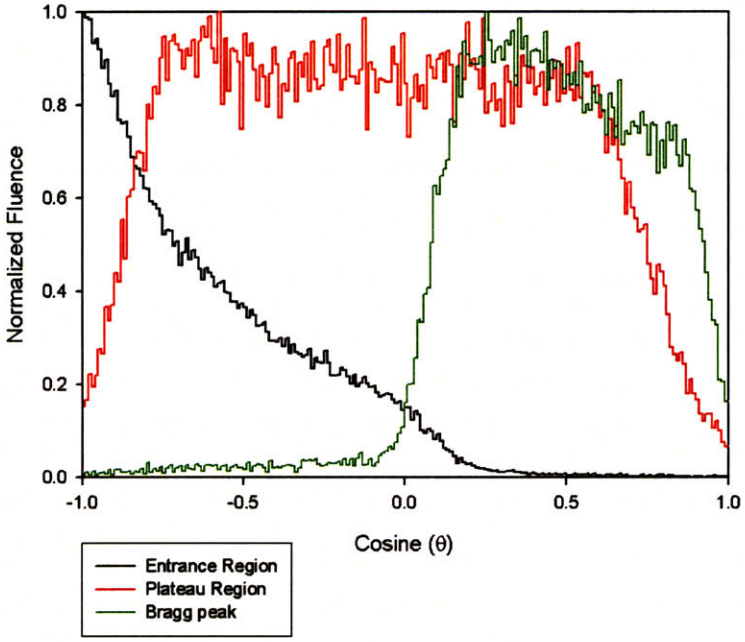

Figure 4-5: Angular distribution of gammas exiting the phantom calculated with GEANT.

Initially it was thought that this may be a problem with the physics packages used with GEANT, but subsequent examination showed that the most up to date physics packages were used for the simulations, and that all angular binning definitions were geometrically correct. The issue is currently under investigation by the Geant4 collaboration.

4.2 MCNPX v2.6.0 – Angular Distribution

Given this problem with GEANT, we decided to examine the angular distribution of gammas with MCNPX, a radiation transport code developed by Los Alamos National Labs. [Pelowitz, 2008] However, MCNPX does not allow for particle-by-particle sampling as GEANT does, so a method had to be developed in order to assess the angular distribution of photons leaving the phantom (ie, we were not able to simply set up an if statement 'if the particle is a photon and exits the phantom, note its trajectory's angle with respect to the proton beam central axis' as we did with GEANT). The phantom was instead divided into regions of Lucite sandwiched between very thin (0.0001cm) void areas with a photon importance of zero. (Figure 4-6)

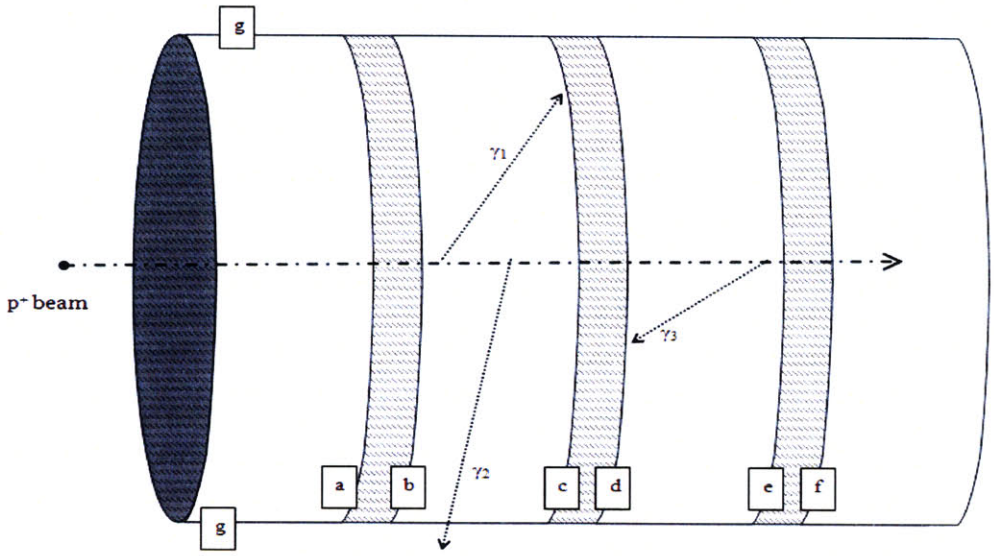

Figure 4-6: Schematic of angular distribution geometry in MCNPX. The shaded regions (between surfaces a&b, etc.) have a photon importance of zero. The proton importance throughout is one. White regions have a photon importance of one. Photons' angular distribution with respect to the proton beam central axis are tallied on each surface. For example, γ_1 is tallied on surface c before being killed in the region between c and d. γ_2 is tallied on surface g. γ_3 is tallied on surface d before being killed in the region between c and d. Not to scale.

The resulting angular distribution calculated by MCNPX was closer to the expected angular distribution described by Kiener *et al.* with a symmetrical distribution about 90° and a local minima at 90°. (Figure 4-7)

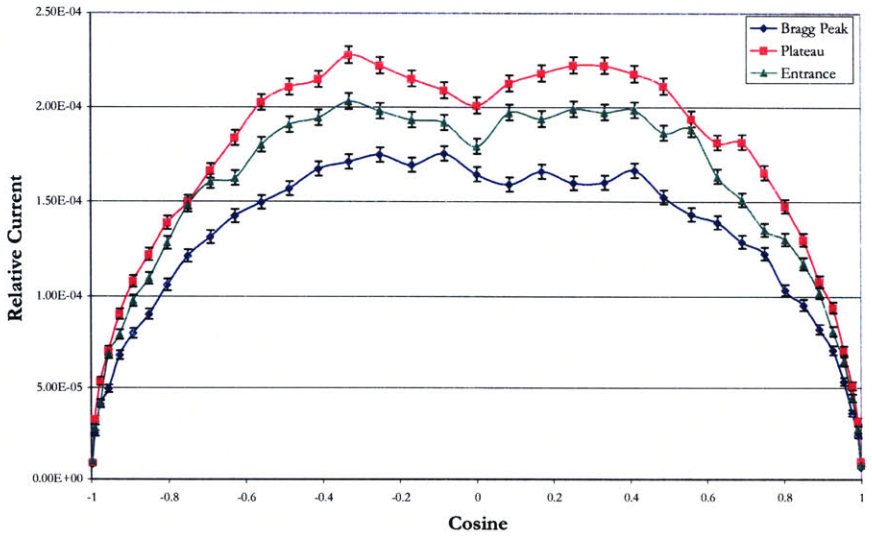

Figure 4-7: Angular distribution of photons exiting the Lucite phantom from MCNPX.

With these promising results, further benchmarking was undertaken to determine whether MCNPX could be used to accurately simulate the physics of prompt gamma production from proton beam therapy.

4.3 MCNPX – FURTHER BENCHMARKING

Two measures were used to determine whether the proton and photon physics simulated with MCNPX were complete enough to simulate the prompt gammas emitted during proton therapy: proton spectrum in phantom, spectrum of photons leaving the phantom.

4.3.1 PROTON ENERGY SPECTRUM

As the proton traverses a phantom, its energy spectrum should broaden, and at the Bragg peak the average energy should be 10-15% of the original beam energy. At the entrance region, the proton energy spectrum should be approximately that of the source.

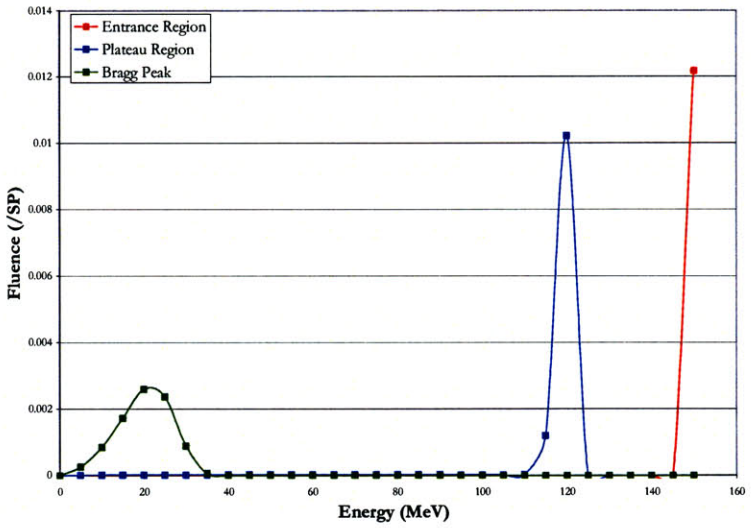

Figure 4-8: Energy spectrum of the proton beam calculated by MCNPX at the entrance region (z=0 cm), plateau region (z=5.5 cm), and Bragg peak (z=14.5 cm). Note the energy broadening from a monoenergetic beam at the entrance region to the broad energy range at the Bragg peak.

The proton energy spectrum calculated by MCNPX behaved as expected, with energy range broadening as the beam loses energy and a peak energy of approximately 10-15% maximum beam energy at the Bragg peak. (Figure 4-8)

4.3.2 GAMMA ENERGY SPECTRUM LEAVING PHANTOM

We demonstrated that the angular distribution of gammas concurs with published experimental data [Kiener, 1998] (at least in the Bragg peak), but it is also necessary that we demonstrate that the photon energy spectrum is correctly simulated by MCNP in order to thoroughly simulate the experimental setup. The most important features that must be present are the characteristic peaks of carbon, hydrogen, and oxygen.

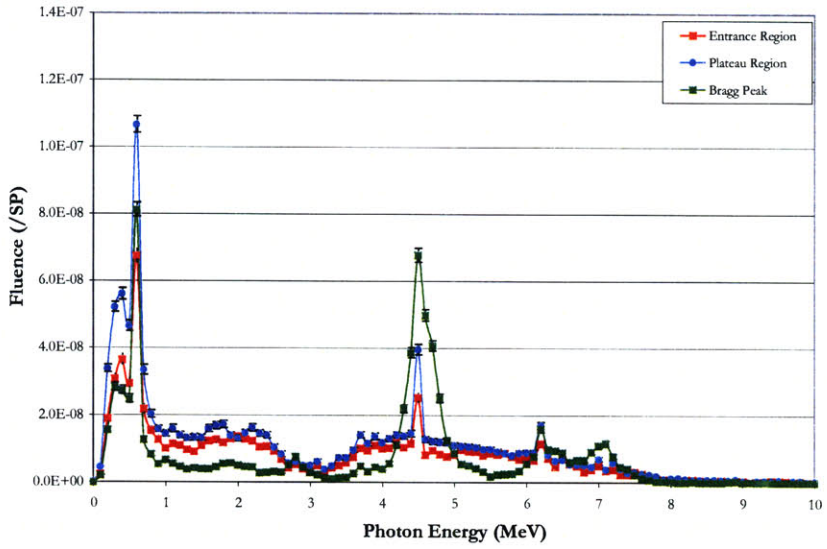

Figure 4-9: Energy spectrum of the gammas exiting the phantom calculated by MCNPX.

As before, a 150MeV proton beam was directed into a Lucite cylinder and the energy spectrum of the exiting photons was recorded. The energy spectrum displayed the expected peaks – 4.44MeV (^{12}C), 2.2MeV (^{1}H), and 6.13 and 7.12MeV (^{16}O). (Figure 4-9) This spectrum, combined with the correct angular distribution and the proton energy spectrum provided sufficient evidence that MCNPX is able to adequately simulate the prompt gamma experiment.

5 HOMOGENEOUS PHANTOM IN MCNPX

5.1 EMULATING THE EXPERIMENTS CONDUCTED AT MGH

When simulating the experiment previously conducted at the Francis H. Burr Proton Therapy Center by Peter Binns and Kent Riley, it was decided that the simulations would emulate ideal conditions and equipment. As a result, only gammas created by the primary proton beam were tracked. In order to obtain the highest signal possible (which ultimately reduces the error associated with the tallies), an annular ring of sodium iodide (NaI) F4 tallies (flux averaged over the cell) surrounded the Lucite QA phantom. (Figure 5-1) Phantom dimensions were identical to the experimental QA phantom. The NaI tallies were arranged orthogonally to the incident proton beam with an internal radius of 25.1cm, an external radius of 26.1cm, and a width of 1cm. In order to obtain the proton depth dose profile, the QA phantom was divided into segments with a length of 5mm along the proton beam path, each of which contained an F6 tally (energy deposition averaged over a cell).

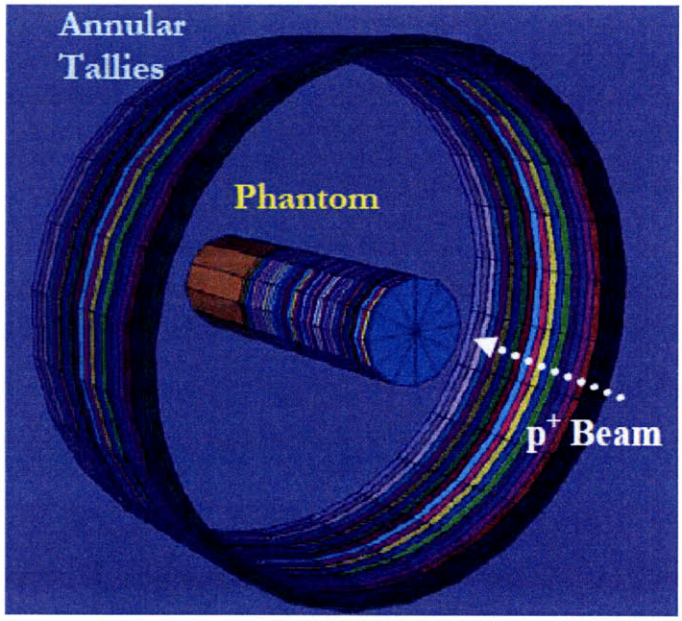

Figure 5-1: 3-D View of Lucite phantom and annular array of NaI tallies (collimators not shown)

In order to ensure that the tallies registered only photons emitted orthogonal to the proton beam central axis, thin (0.0001cm) ideal collimators were placed between each NaI ring, extending from the phantom to the annular NaI. (Figure 5-1) Tallying was conducted from 0 – 20MeV with increments of 100keV. A 147.5MeV monoenergetic proton pencil beam was delivered to the

Lucite phantom.* Approximately 103 million source particles (protons) were required to obtain uncertainty of <1% for the total gamma fluence detected in the NaI tallies. Run time was approximately 2635 minutes.

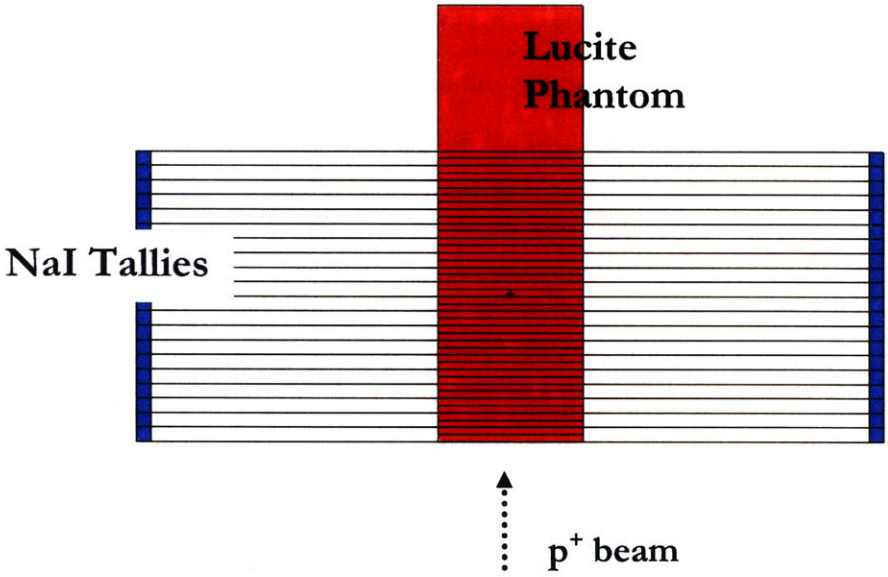

Figure 5-2: 2-D View of the phantom (center, red, diameter=10.2cm), NaI tallies (sides, blue) and collimators (lines extending from phantom to tallies). Proton beam enters phantom from the bottom of the figure. Drawn to scale.

The gamma emission profile yielded a total integral photon emission peak 2±0.5cm proximal to the Bragg Peak, with plateau emissions ranging from 70%-90% of the peak. Spectrographic data from the tallies revealed that the most abundant gamma emission near the Bragg peak was the 4.44MeV peak from ^{12}C, likely due to the high percentage of carbon in Lucite. (Figure 5-3)

* 147.5 MeV proton beam emulates the 150MeV at-nozzle-entrance proton beam used during the experiments. The 150MeV passed through 2m of air, losing approximately 2.5MeV before entering the QA phantom.

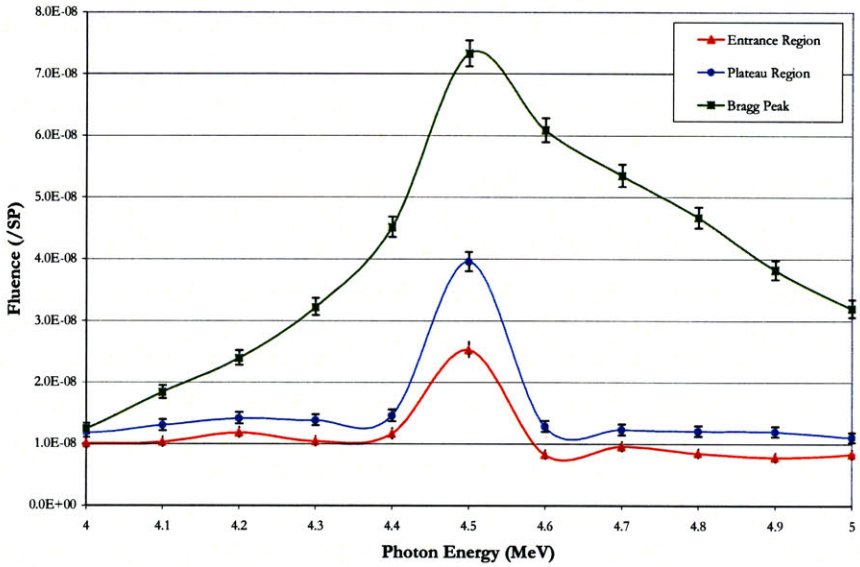

Figure 5-3: Energy spectrum of the gammas detected in the annular tallies, 4-5MeV. Note that the fluence at the Bragg peak at 4.5MeV is nearly a factor of 2 greater than other regions of the phantom.

Arbitrary integration about this energy (4-5MeV, as well as 4-8MeV, which was the energy range examined during the initial experiments) was conducted. Both sets of binned data yielded an emission peak at about 1±0.5cm proximal to the Bragg peak, with plateau emissions ranging from 40%-70% and 30%-60% of the peak for the 4-8MeV and 4-5MeV gamma data, respectively. (Figure 5-4)

This difference in peak position relative to the Bragg peak for the total and energy binned data is to be expected – examining Figure 4-9 reveals that there is an abundance of low energy gammas (large 400keV and 600keV peaks) particularly prominent in the plateau region, ultimately raising the number of counts in the plateau region. 4-8MeV and 4-5MeV energy binning discounts these low energy gammas, reducing the number of plateau counts without affecting the number of Bragg peak counts.

The 4-5MeV data yielded the cleanest emission peak, with the highest peak to plateau gamma fluence ratio. However, when compared to the total gamma fluence, narrowing the energy range over which the fluence is integrated lowers the total number of counts received per Gy delivered

in the Bragg peak area. With this geometry, the total integral fluence to the 4-8MeV integrated fluence ratio was approximately 1.9:1, whereas the total integral fluence to the 4-5MeV integrated fluence ratio was approximately 3.4:1.

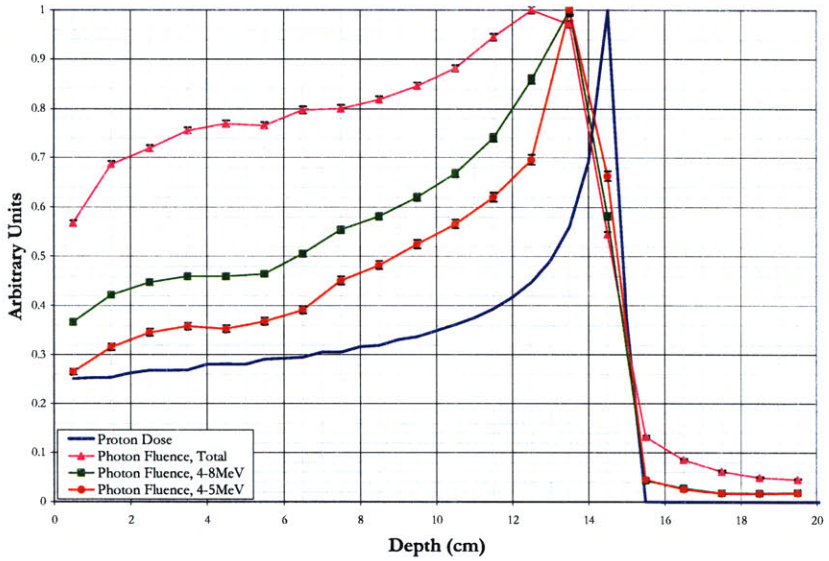

Figure 5-4: Emission spectra as a function of depth in the phantom along the beam path. 4-5MeV and 4-8MeV integrated and total integral fluences plotted. Proton depth dose profile included, with the Bragg peak at a depth of z=14.5cm.

While this is a relatively minor issue for these simulations which may simply run for longer durations in order to achieve acceptable statistics, or even for an experiment, in which proton beam time or current could be increased in order to obtain more gamma counts, it is a concern for clinical scenarios in which a decreased fluence results in larger errors, and simply increasing the dosage to obtain more counts is not an acceptable solution. However, the results indicate that, while there is a significantly lower gamma fluence when energy binning is conducted, a $1cm^2$ detector with 100% efficiency and 4-5MeV energy binning and 1Gy delivered at the Bragg peak would yield a count of 613 photons and, according to Poisson statistics, an error of 4.1%. (Figure 5-5)

Dose delivered at the Bragg Peak was determined by placing a small cylindrical F6 tally (2cm x 1cm, radius x width) in the homogeneous Lucite phantom at z=14-15cm centered on the proton beam central axis, resulting in a volume of π cm^3 with a mass of 3.738g. Using the conversion $1MeV = 1.060217646x10^{-13}J$, and 1Gy=1J/kg, the dose deposited in the volume per source

particle was determined. [Turner, 2004] Each proton source particle delivered 6.96×10^{-10}Gy to the target area, correlating to 1.44×10^{9} source protons per Gy deposited.

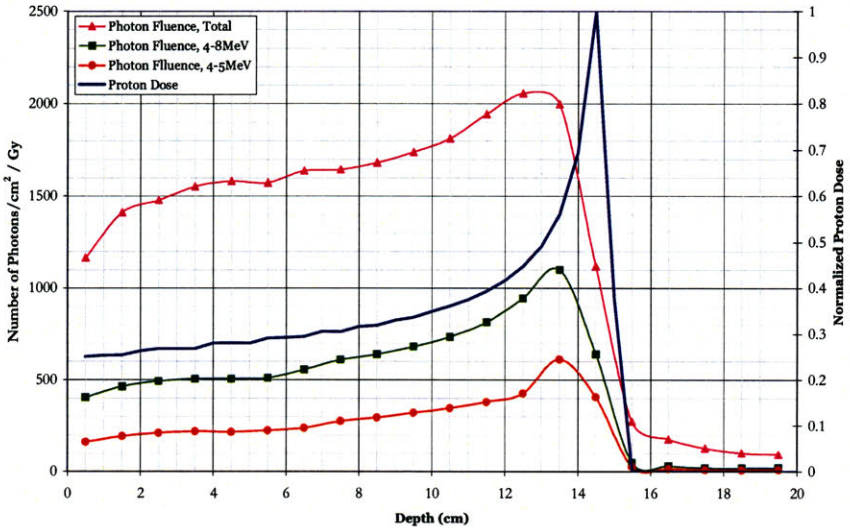

Figure 5-5: Fluence as a function of depth in phantom for a 1cm2, 100% efficient detector and 1Gy proton dose delivered at the Bragg peak. Depth dose profile plotted for reference.

Computational results compare well to experimental emission peak results, which also yielded a peak approximately 2-3cm proximal to the Bragg peak. Measured gamma emissions proximal and distal to the emission peak, however, vary greatly from those computed by MCNPX, likely due to the noise in the experiments. (Figure 5-6) Statistical uncertainty was relatively low (in most cases <2%) for MCNPX calculations.

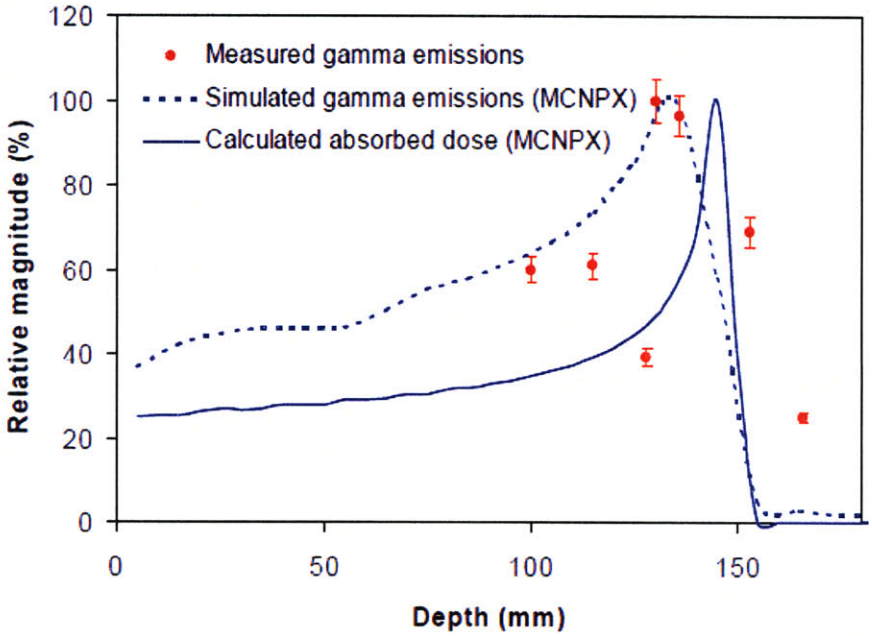

Figure 5-6: Gamma emissions measured as a function of distance along Lucite cylinder for an incident 150MeV proton pencil beam plotted together with an MCNPX calculated profile.

5.2 200MeV Proton Beam

As Figure 3-1suggests, the prompt gamma production cross section peaks at a proton energy of approximately 10-11MeV. While this falls at or slightly distal to the Bragg peak for the 147.5MeV proton beam used in our initial simulation, this is not the case for all energies.* In order to examine the effect that higher energy beams have on the gamma emission spectra, the 147.5MeV beam was replaced with a 200MeV proton beam. This higher energy beam will have a slightly broader proton energy spectrum at the Bragg peak than the 147.5MeV, with an average energy of approximately 20MeV.

The geometry used with the 147.5MeV proton beam was modified to account for the greater penetration of the beam (the Bragg peak for the 200MeV beam was located at z=24.5cm, whereas it was located at z=14.5 for the 147.5MeV beam). Material composition, beam

* As a rule of thumb, the average proton energy at the Bragg peak is equal to approximately 10% of the average energy of the entrance beam.

characteristics (besides energy), physics settings, and detector/collimation schemes remained unchanged.

Approximately 26 million source particles were required to obtain uncertainty of ~2% for the total gamma fluence detected in the NaI tallies. Run time was approximately 767 minutes.

The simulation yielded results similar the E_p=147.5MeV simulation – the 4-5MeV and 4-8MeV data displayed an emission peak approximately 1cm proximal to the Bragg peak, while the total fluence emission peak was located 2cm proximal to the Bragg peak. (Figure 5-7) This curious result is likely a result of the spatial resolution of our simulation geometry. Given that the NaI tallies have a width of 1cm, the maximum achievable resolution is approximately 1cm. While the average position of the 10-15MeV protons may be slightly closer to the Bragg peak from the 200MeV beam compared to the 147.5MeV beam, this movement is not on the order of 1cm, and was therefore undetectable by our geometry.

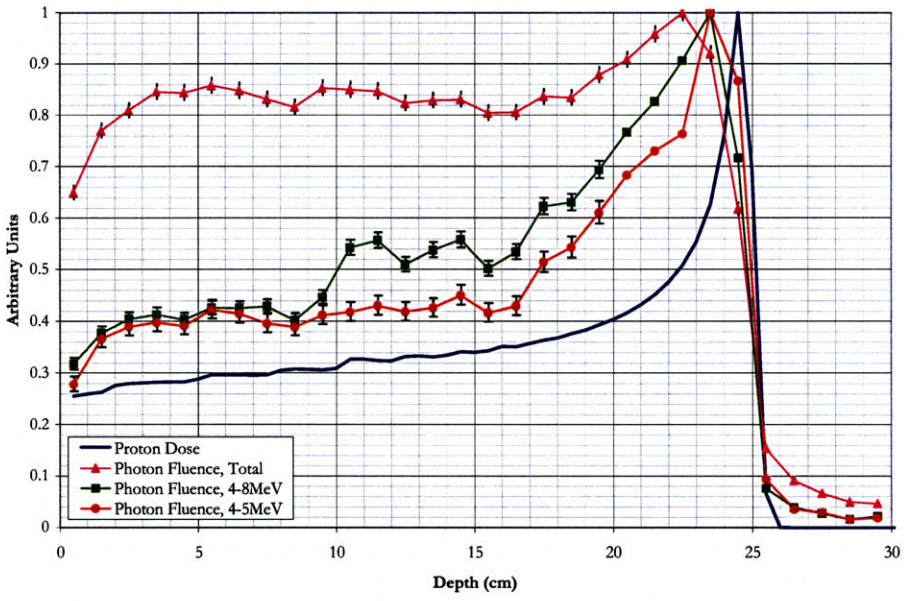

Figure 5-7: Emission spectra as a function of depth in phantom along the beam path for 200MeV proton beam.

5.3 EFFECT OF SEED IMPLANT ON SIGNAL

Metal implants are not uncommon in radiation therapy patients. Quite often the spinal canal needs Titanium screws for support after tumor mass has been removed surgically. The implantation of a metal seed into the phantom was our first foray into phantom inhomogeneities. Both titanium and gold seeds were simulated, with dimensions of 0.08cm x 0.3cm (diameter x length), which were placed at z=5-5.3cm (the plateau region of the depth dose profile) directly along the central axis of the proton beam. All other phantom and detector geometry and physics were identical to that described in Section 5.1. A 147.5MeV proton beam was used. (

Figure 5-8)

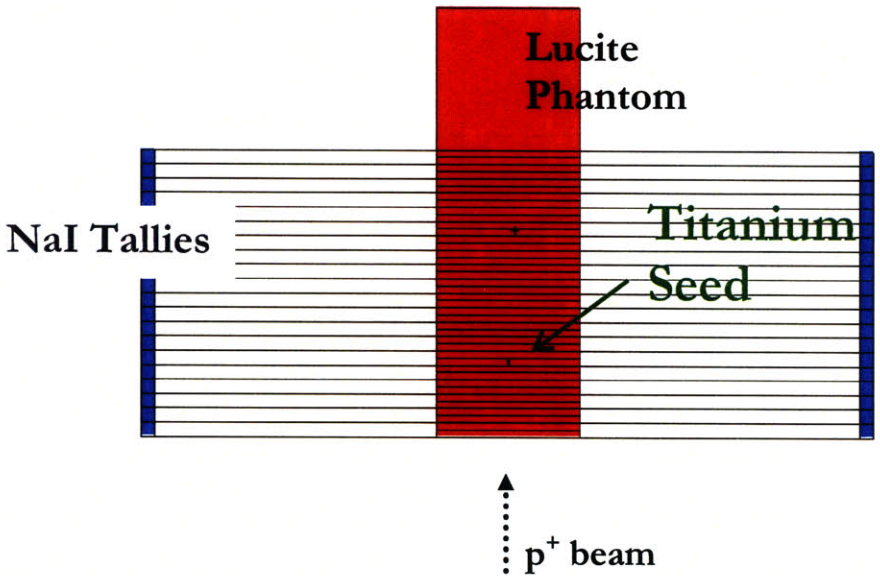

Figure 5-8: 2-D view of phantom (diameter 10.2cm), NaI tallies, collimators, and implanted Ti seed. Shown to scale.

Approximately 86 million source particles were required to obtain uncertainty of ~2% for the total gamma fluence detected in the NaI tallies. Run time was approximately 2735 minutes.

The energy spectrum at the entrance region and at the Bragg peak was nearly identical to the spectrum of the phantom sans implanted seed. The energy spectrum at the seed position,

however, displayed a significant increase in the number of low energy counts registered, with new low energy peaks corresponding to the characteristic peaks of the seed materials. (Figure 5-9)

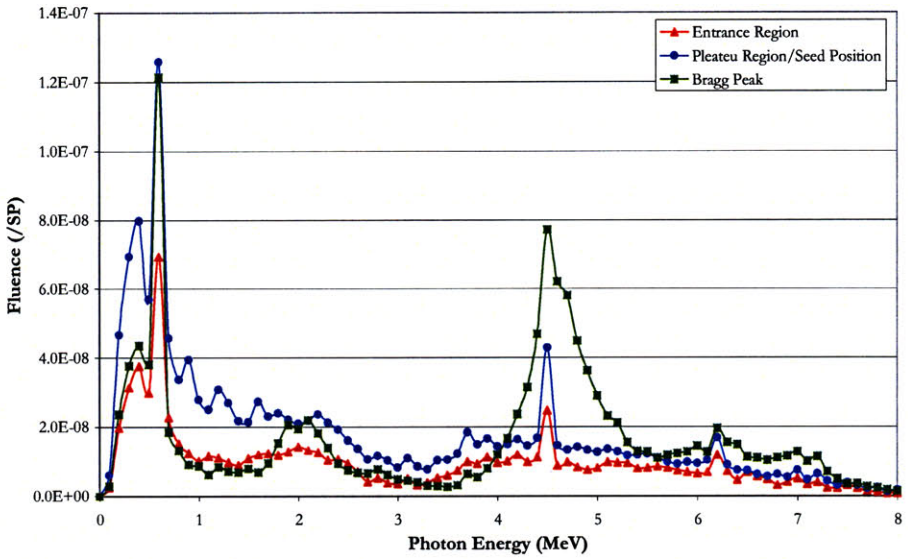

Figure 5-9: Energy spectrum of the gammas detected in the annular tallies. Ti seed implanted at z=5.0cm

This increased low energy gamma fluence resulted in a total emission peak at the location of the implanted seed. Energy binning, however, yielded emission spectra not dissimilar to those seen in Figure 5-4. Energy binning filtered the low energy gammas produced in the seed, resulting in an emission profile similar to a Lucite phantom without an implanted seed.(Figure 5-10) While slight local emission maxima can be observed at the seed location, the 4-5MeV and 4-8MeV data still display a prominent peak 1cm proximal to the Bragg peak. This was the first time the benefits of choosing an energy binning scheme such that the emission peak to plateau ratio is maximized was fully realized. This result suggests that, with energy binning, the presence of a metal implant should not prevent this technique from being used on a patient. It does not, however, suggest that a metal implant could be used in conjunction with the prompt gamma detection technique in order to better assess the proton beam range.

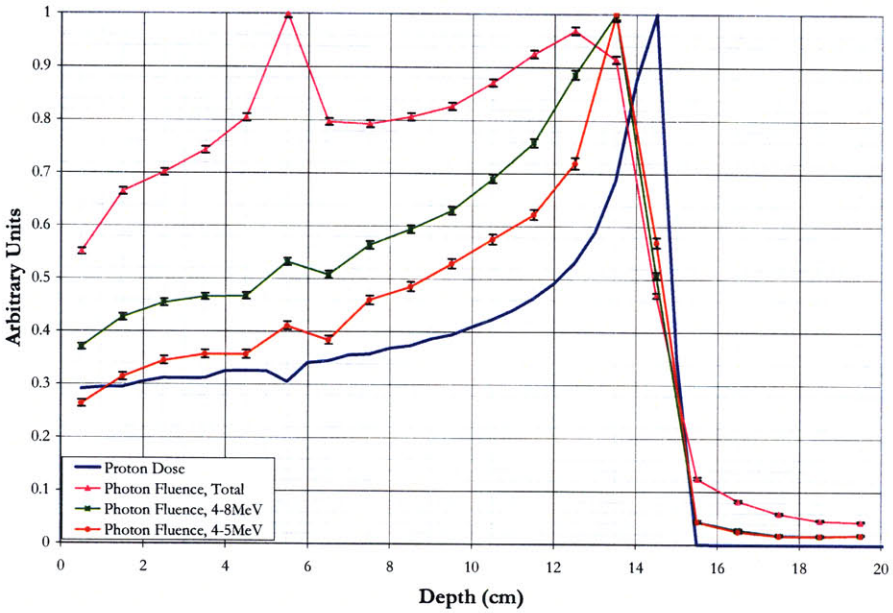

Figure 5-10: Emission spectra as a function of depth in the phantom along the beam path. Ti seed implanted at z=5.0cm.

5.4 COMMONALITIES

The implanted seed geometry made apparent that energy binning with respect to gamma peaks that are preferentially abundant at the Bragg peak can help to filter the signal and obtain a clear emission peak near the Bragg peak.

Interpolation between data points revealed that in all Lucite phantom simulations the position of the 50% distal falloff in photon intensity for the 4-8MeV data correspond with the position of the 80% distal falloff of the Bragg peak. While the poor (1cm) spatial resolution of the detector geometry prevents us from concluding that this relationship always exists, it is an intriguing correlation which should be studied further and may prove useful in clinical setups.

6 HETEROGENEOUS PHANTOM IN MCNPX

6.1 DESCRIPTION OF HETEROGENEOUS PHANTOM

In order to assess the possible effect that tissue inhomogeneities might have on the gamma signal, a heterogeneous phantom was simulated which consisted of bone and lung equivalent materials and poly-methyl methacrylate (PMMA). The slabs were arranged to form air-lung, air-bone, and lung-bone interfaces which were positioned parallel or at a 6° angle relative to the PMMA slabs. The phantom also contained an arrangement of six metal implants, two of which were authentic dental gold implants, and the remaining four were composed of a tin lead alloy. This particular phantom was chosen because it was developed and constructed in house at MGH for a proton/PET study, and is readily available for experiments. [Knopf, 2008]

Table 6-1: Elemental composition (fraction by weight) and density of the PMMA and tissue equivelent materials. [Knopf, 2008]

Medium	H (%)	C (%)	N (%)	O (%)	Mg (%)	Cl (%)	Si (%)	Ca (%)	ρ (g/cm^3)
PMMA	8.05	59.99	-	31.96	-	-	-	-	1.18
Bone Eq.	3.41	31.41	1.84	36.5	-	0.04	-	26.81	1.82
Lung Eq.	8.46	59.38	1.96	18.14	11.19	0.10	0.78	-	0.30

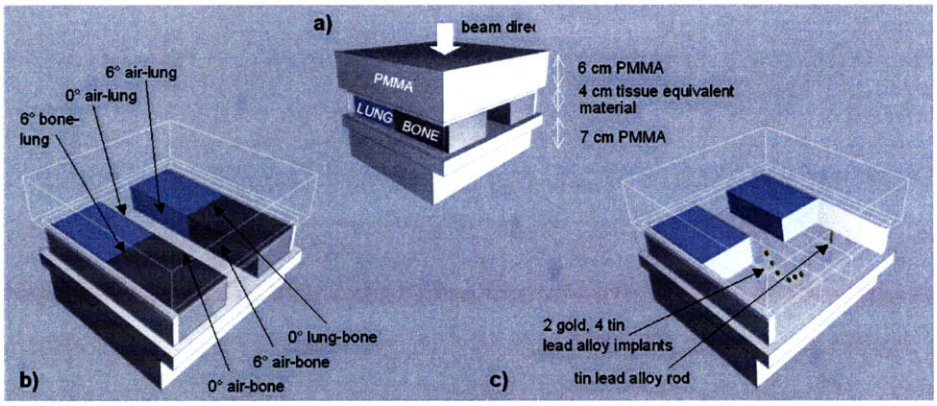

Figure 6-1: Drawing of MGH's in-house designed heterogeneous phantom

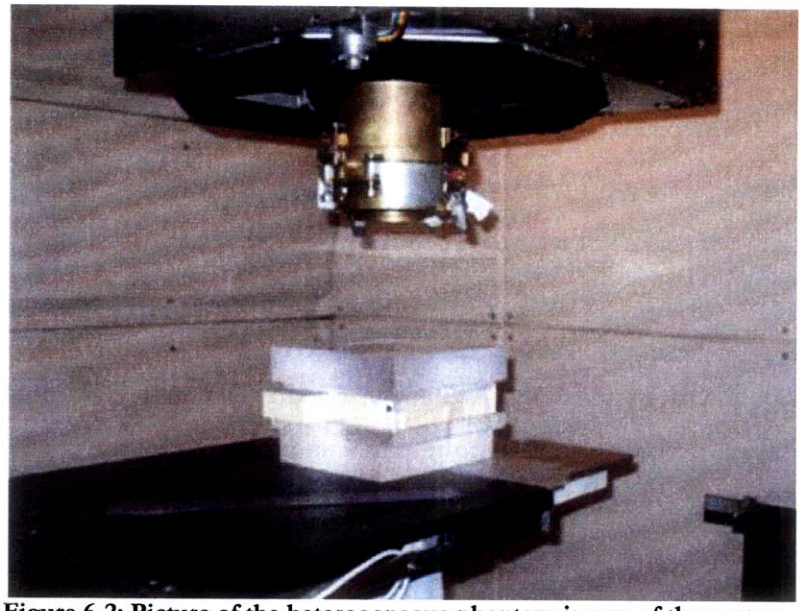

Figure 6-2: Picture of the heterogeneous phantom in one of the proton beam gantries at the Francis H. Burr Proton Therapy Center. [Knopf, 2008]

The tallying scheme used was similar to that used on the Lucite phantom. An annular ring of NaI F4 fluence tallies surrounded the heterogeneous phantom, which were arranged orthogonal to the proton beam central axis with an internal radius of 25.1cm, and external radius of 26.1cm, and a width of 1cm. In order to obtain the depth dose profile of the proton beam in the phantom, sections of the phantom which ran along the proton beam path were divided into 2cm x 0.5cm (diameter x length) cylinders, each of which contained an F6 energy deposition tally. (Figure 6-3)

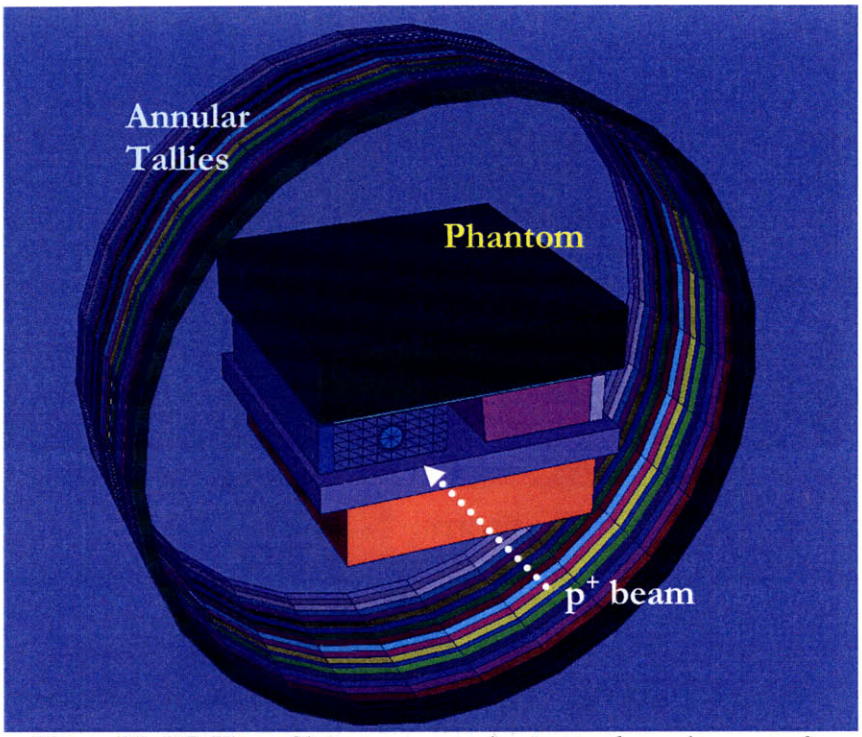

Figure 6-3: 3-D View of heterogeneous phantom and annular array of tallies (collimators not shown). Note the small round section of the phantom - the portion sectioned off to obtain the proton depth dose profile.

Similar to the Lucite phantom simulations, thin (0.0001cm) ideal collimators were placed between each NaI tally in order to ensure that only photons emitted orthogonal to the proton beam were tallied. Given that the heterogeneous phantom is not cylindrically symmetric about the proton beam central axis, these collimators could not extend from the phantom to the tallies. Instead, they came as close as possible to the phantom, touching the phantom's corners, with an internal radius of 16cm and an external radius of 25.1cm. Note that the annular tallies are not centered about the proton beam's central axis, but the center of the phantom. While this is not the ideal scenario, this geometry provided the maximum collimator length, and still was able to effectively tally gammas emitted orthogonal to the proton beam effectively. (Figure 6-4)

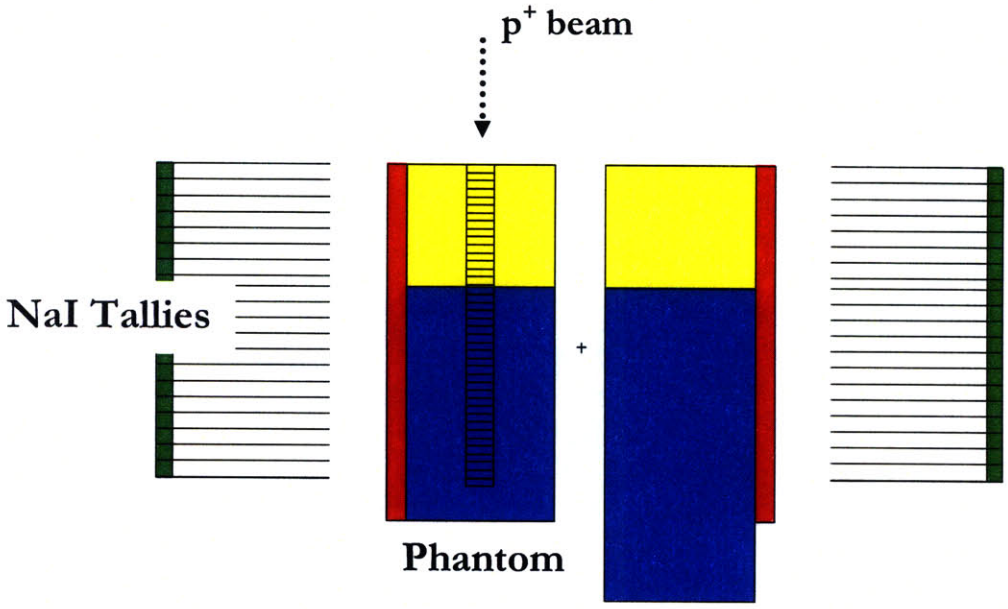

Figure 6-4: 2-D View of the heterogeneous phantom in which the beam enters lung (yellow) and stops in bone (blue) equivalent materials. Phantom also includes PMMA (red), surrounded by NaI tallies (green) and collimators (lines extending from the NaI). Note the segments used to determine the depth dose profile of the proton beam.

While there were a number of available scenarios that could be examined with this phantom, only two were simulated: the proton beam entering bone and stopping in lung equivalent material, and the proton beam entering lung and stopping in bone equivalent material. This was chosen over also including PMMA (which is often used as a tissue equivalent material for radiological studies) because the bone and lung equivalent materials represent the highest and lowest density materials, respectively, providing the greatest contrast between two materials. The implanted seeds were not used because the effect that an implanted seed has on the gamma signal was already examined with the Lucite phantom, and the main goal was to study the effect that inhomogeneities in tissue composition have on the gamma signal.

6.2 PROTON BEAM: LUNG → BONE

The first simulation conducted used a heterogeneous phantom geometry in which the proton beam passed through 7.6cm of lung equivalent material before stopping in bone equivalent material. The Bragg peak occurred at $z \approx 17$cm, with an approximate range of 10.4cm in the bone

equivalent material. A 147.5MeV proton beam was delivered. Approximately 5 million source particles were required to obtain uncertainty of <10% for the total gamma fluence detected in the NaI tallies. Run time was approximately 255 minutes.

Spectrographic data from the tallies revealed that, once again, the most abundant gamma emission peak near the Bragg peak was the 4.44MeV peak from ^{12}C. It should be noted that there were other peaks which were more abundant at the Bragg peak than in other areas along the depth dose profile in the phantom, including gamma energies of 2.2, 2.9, and 3.8MeV. While the photon count at these energies was significantly higher than at the same energy for other regions of the phantom, these peaks were isolated. The 4-5MeV range not only included the prominent 4.44MeV peak, but was also the largest range over which the photon counts at the Bragg peak was consistently higher than at other areas of the phantom. As a result, integration of the 4-5MeV data was conducted. (Figure 6-5)

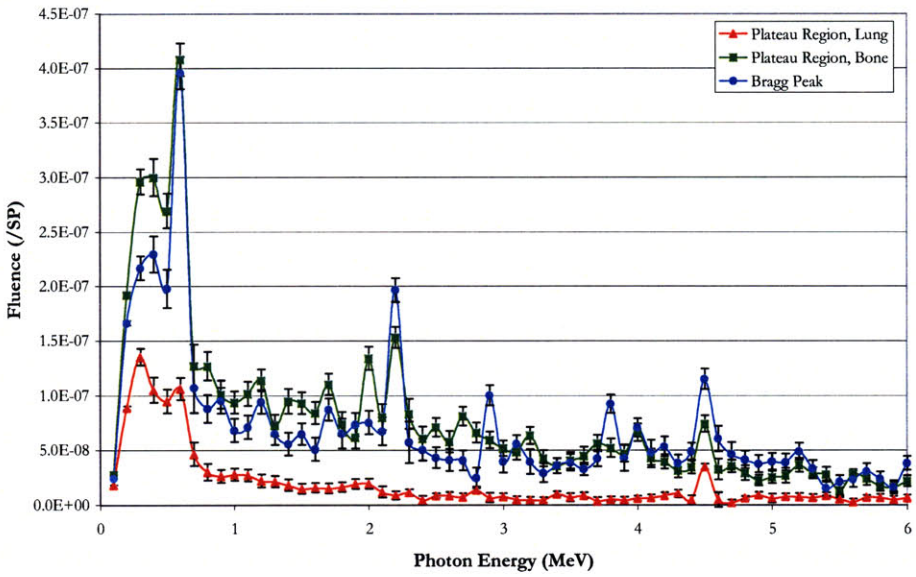

Figure 6-5: Energy spectrum of the gammas detected in the annular tallies, 0-6MeV.

The normalized data revealed that both the total gamma fluence tallies and the 4-5MeV fluence yielded emission peaks approximately 1.5±0.5cm proximal to the Bragg peak. Figure 6-6 reveals that the fluence in the lung region was significantly lower than in the bone region, mostly due to

the difference in density between the bone and lung equivalent materials (bone equivalent material is a factor of 6.1 more dense than lung equivalent material). The 4.5MeV data had a higher peak to plateau ratio, displaying a more distinct peak.

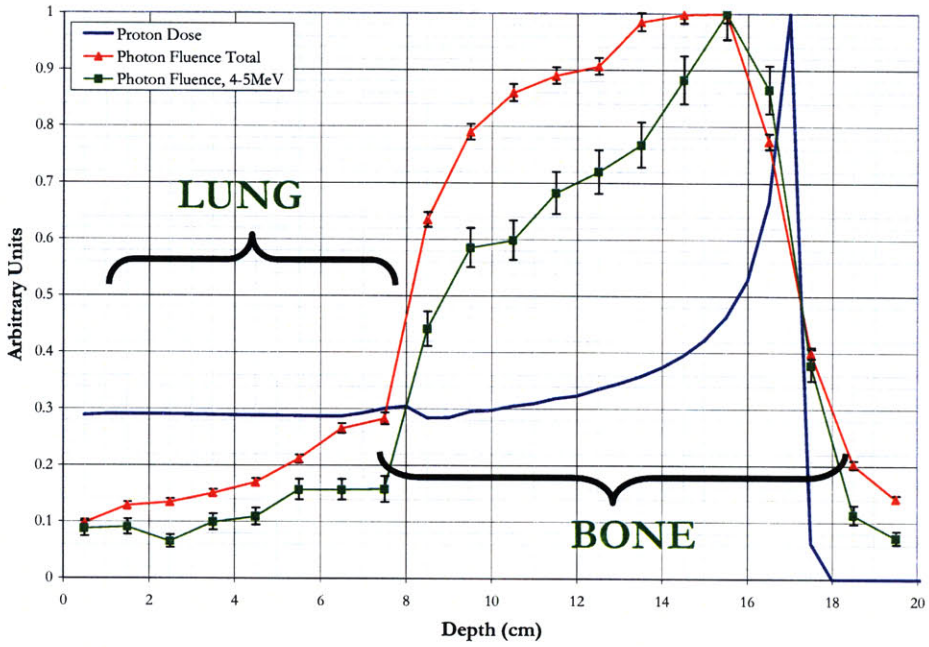

Figure 6-6: Normalized emission spectra as a function of depth in the phantom along the beam path. Note the lung and bone equivalent regions (z=0-7.6cm and z>7.6, respectively)

As may be assumed by the higher error bars in the 4-5MeV data when compared to the total fluence data, the 4-5MeV data received fewer counts. Just as with the Lucite phantom, narrowing the range over which the fluence is integrated lowers the total number of counts received per Gy delivered to the Bragg peak area. The total fluence tallies recorded approximately 10 times more counts than the 4-5MeV tallies. (Figure 6-7)

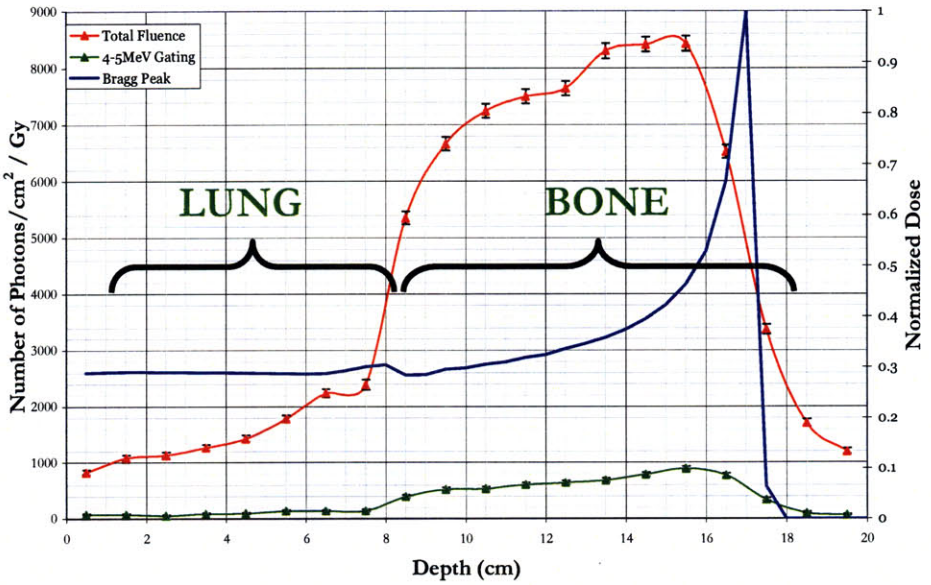

Figure 6-7: Fluence as a function of depth in phantom for a 1cm², 100% efficient detector and 1Gy proton dose delivered at Bragg peak. Depth dose profile plotted for reference.

While the relatively low number of counts may present a problem for clinical implementation it was not an issue for these simulations, and the data show that, for the given geometry, a peak can be measured in the gamma emission profile which correlates with (but is not at the location of) the Bragg peak.

6.3 PROTON BEAM: BONE → LUNG

The second simulation conducted using a heterogeneous phantom switched the positions of the lung and bone equivalent slabs. In this case the proton beam passed through 7.6cm of bone equivalent material before stopping in lung equivalent material. (Figure 6-8) The Bragg peak occurred at $z=17.5\pm0.25$cm, with an approximate range of 11.5cm in the lung equivalent material. In order to use the same detector geometry used in the Lung→Bone study, the proton beam energy was reduced to 140MeV (otherwise the proton beam would have passed beyond the final NaI tally). Approximately 41 million source particles were required to obtain uncertainty of

~2% for the total gamma fluence detected in the NaI tallies. Run time was approximately 1202 minutes.

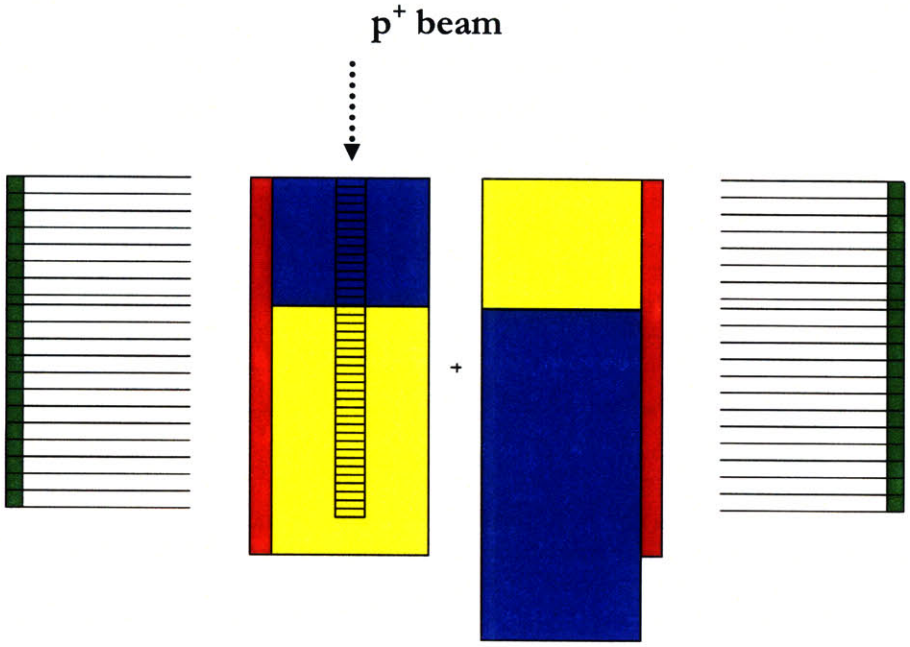

Figure 6-8: 2-D View of the heterogeneous phantom in which the proton beam enters bone (blue) and stops in lung (yellow) equivalent materials.

Spectrographic data revealed that the integral photon flux from bone equivalent material was higher than from the lung equivalent material at every **z** position, and at every photon energy. (Figure 6-9)

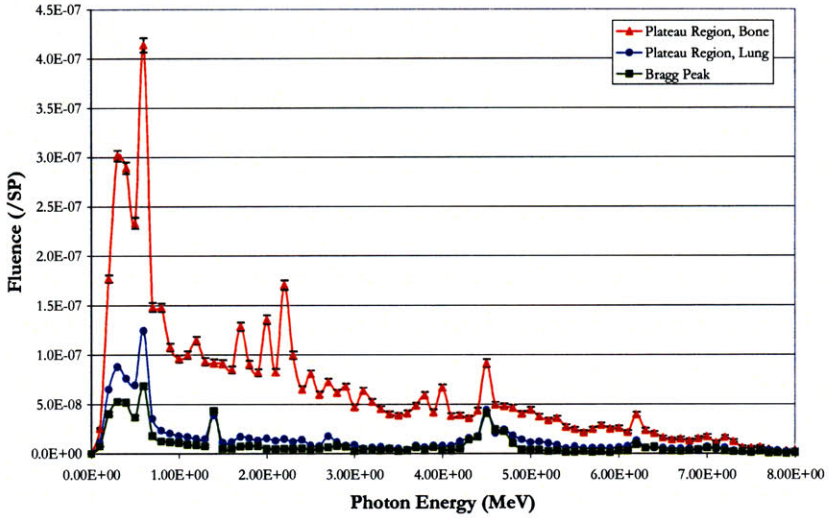

Figure 6-9: Energy spectrum of the gammas detected in the annular tallies, 0-8MeV

As a result, the strategy used prior (finding a peak, namely 4.44MeV, which is preferentially higher in the Bragg peak region than in all other locations) would not work, as there is no energy at which the Bragg peak region emits a higher gamma fluence than any other region in the phantom. Instead, only the emission and energy spectrum in the lung equivalent material region were considered.

Upon closer inspection, it was revealed that there was one peak (1.4MeV) at which a slightly higher fluence is detected in the Bragg peak region than in the rest of the lung equivalent slab. This is likely the 1.37MeV line from ^{24}Mg, which makes up 11.19% (by weight) of the lung equivalent slab, and is not present in the bone equivalent slab. (Figure 6-10)

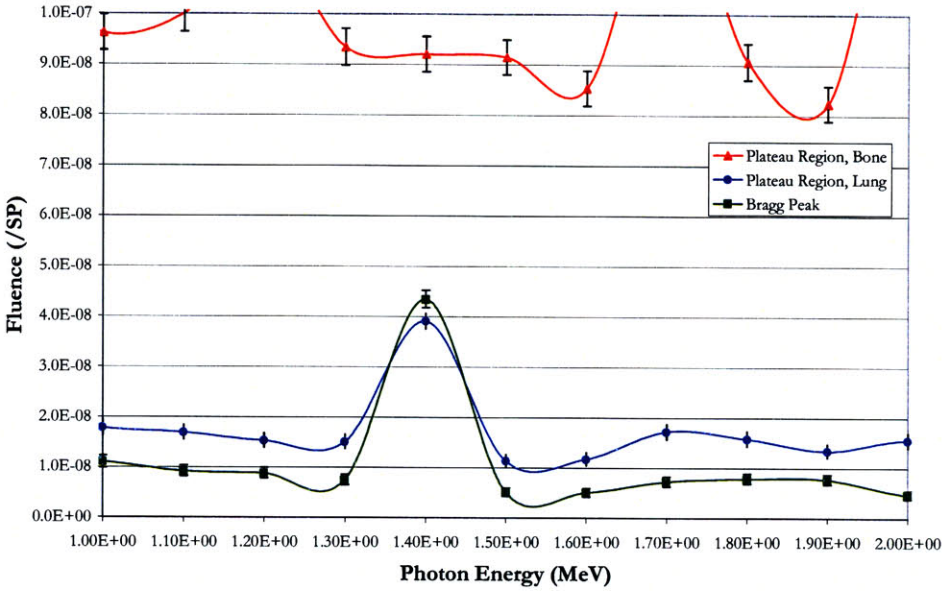

Figure 6-10: Energy spectrum of the gammas detected in the annular tallies, 1-2MeV. Note the slight difference between the plateau and Bragg peak regions at 1.4MeV.

The data normalized to the highest fluence in the entire phantom displayed global maxima for both the total fluence and 1.4MeV fluence, with the 1.4MeV data also displaying a local maxima 1±0.5cm proximal to the Bragg peak. When renormalized to take into account only fluence emitted from the lung equivalent slab, this maxima 1±0.5cm proximal to the Bragg peak becomes more prominent. (Figure 6-11)

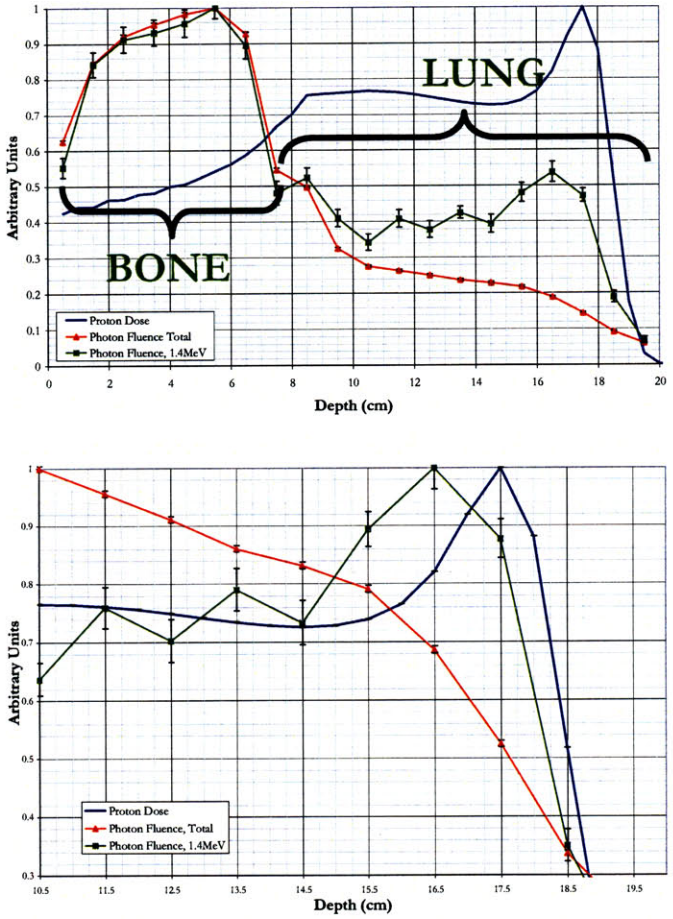

Figure 6-11: Normalized emission spectra as a function of depth in the phantom along the beam path. Top: Normalized to the peak fluence from all points in the phantom. Bottom: Normalized only to lung region.

This binning strategy suggests that understanding the composition of the tissue/material in which the proton beam stops is critical, especially when there is a great difference in density between the two materials. In such a case, one must take into account the density of a particular isotope of interest.

For example, the lung equivalent material had a greater percentage of carbon, by weight, than the bone equivalent material in the heterogeneous phantom. However, when one takes the density of each material into account, the density of carbon in the lung equivalent material is 0.17814g/cm^3,

while the carbon density in the bone equivalent material is 0.571622g/cm^3, a difference of a factor of 3. As a result, the 4.44MeV peak was more abundant in the bone slab.*

In this case, it was necessary to perform energy binning in the Bragg peak area, suggesting that particularly inhomogeneous geometries in which it is uncertain in what material the proton beam stops, require a more advanced filtering method than those examined for this study. However, this study suggests that it is possible to determine the range of a proton beam based on the prompt gamma emission profile, provided the material in which the beam stops is known.

While this presents a difficulty in implementing this technique clinically, it is not impossible. Algorithms are already in use which correlate each voxel in a CT to a particular tissue type based on the Hounsfield reading in that area. With this technique, it could be determined what types of tissues a proton beam will traverse for a given gantry angle, allowing physicists to predict the observed gammas and conduct energy binning accordingly.

* Its abundance is not greater by a factor of 3 with respect to the abundance in the lung equivalent material because the higher energy proton beam in the bone equivalent material has a smaller 4.44MeV gamma cross section than does the lower energy proton beam in the lung equivalent material. Had the 4.44MeV gamma production cross section not been a function of proton energy, the 4.44MeV gamma emission from the bone would have been 3.203(=0.571622$_{g/cc}$/0.17814$_{g/cc}$) times higher than the emission from the lung equivalent material.

7 FUTURE WORK

7.1 EXPERIMENTAL

The first round of experiments conducted at the Francis H Burr Proton Therapy Center were little more than an attempt to reproduce the results published by Min, *et al.* The results of those experiments do reveal a correlation between the gamma emission profile and the depth dose profile of the proton beam, but they also include some anomalies, including an unexpected fluence dip approximately 10cm proximal to the Bragg peak, and a significant photon fluence distal to the Bragg peak. Further experiments must be conducted in order to determine the cause of these anomalies, and how they may affect the overall viability of prompt gamma emission detection as a means of proton beam range verification.

In addition, while the simulations described above have provided a wealth of information as to the potential signals we may receive from different types of geometry and material compositions, all of this must be verified experimentally. Our MCNPX simulations represent an idealized world in which detectors are 100% efficient, collimators are thin and stop any extraneous particle that collides into them, and in order to obtain acceptable statistics we need only dedicate more computer time to the simulation. It needs to be determined whether the energy binning techniques provide a large enough signal for a clinically relevant number of monitor units, or whether other means of signal filtration may provide a greater SNR.

One potential means of filtering may be to examine angled collimators, examining gammas emitted at some angle θ (where $\theta \neq 90°$, as that scenario has already been examined). Recall from Figure 4-4 that the gamma emittance differential cross section reaches a maximum at 30°-40°. Using an angle at which more gammas are emitted would lead to a greater number of counts registered in a detector, ultimately yielding a higher SNR.

7.2 COMPUTATIONAL

While the importance of experimental validation is crucial to determining whether the idealized MCNPX results correspond to meaningful real-world results, there is an abundance of future simulations which should be conducted to aid experimental work and examine clinical settings.

MCNPX could be used to optimize the experimental setup, by examining various collimation widths, collimation lengths, dimensions of shielding, distance of detectors from phantom, distance between detectors, collimator angle, etc. This is a task more easily simulated than experimentally tested, and would likely reduce the number of experiments necessary to obtain meaningful experimental validation and move to a more clinical focus for this study. Simulations should also be undertaken which have a finer spatial resolution around the position of the maximum gamma emission in order to more accurately correlate the emission peak with the Bragg peak.

In addition, simulations could be conducted which examine a more clinically relevant target phantom. Instead of examining slabs of tissue equivalent materials, we could instead examine more lifelike geometries. Numerous options are available, from the relatively simplistic Oak Ridge National Laboratory mathematical model phantom, to the more complex voxelized VIP Man developed at the Renssealer Polytechnic Institute. [Guatelli, 2005] [Jiang, 2005] (Figure 7-1) Simulations could be developed which mimic an actual treatments, resulting in a spectrum representative of what we should expect when we scan a patient.

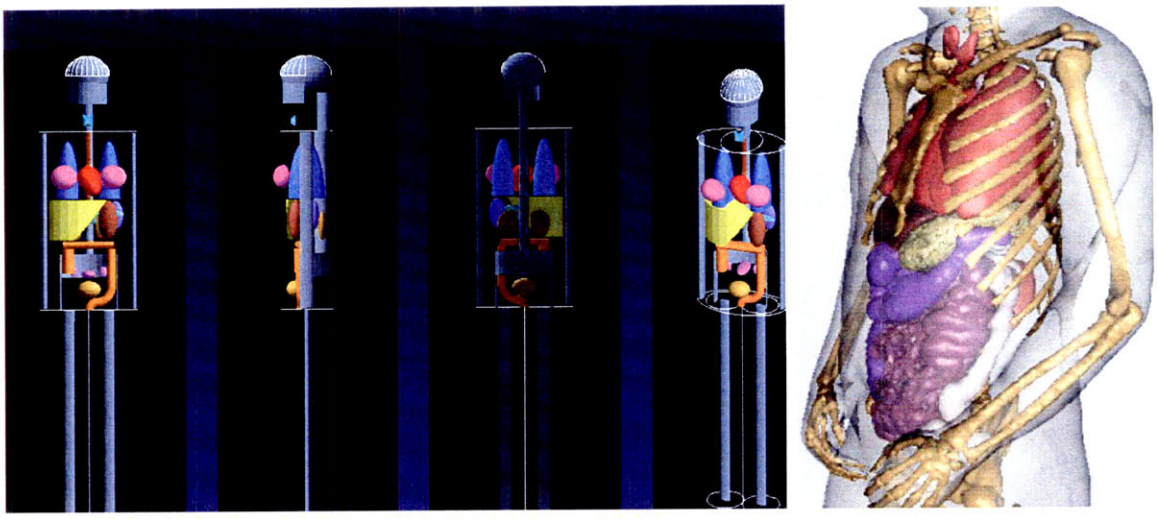

Figure 7-1: ORNL female phantom (left) and VIP voxelized phantom (right)

Work should also continue to determine the source of the problems with our implementation of GEANT4.8.0 (or of GEANT itself), and why it is currently failing to accurately represent the correct angular distribution of the emitted gammas. Current collaboration with Tatsumi Koi at the Stanford Linear Accelerator Laboratory is promising. Recent work has shown that the use of the `GetMomentumDirection` function (as opposed to the geometrical means we had used before, see Appendix B) for photon tracking has yielded gamma angular distributions which are consistent with published data and MCNPX simulations.

If we are able to resolve this problem, we would be able implement an actual treatment beam and real patient CTs, as the programs have already been developed which incorporate the patient CT information and treatment plan into GEANT. Ultimately, this may allow us to scan the gammas emitted from a patient and, using that patient's CTs and treatment plan input into GEANT, simulate the gamma emittance as well. Such studies would also help develop a quantitative correlation, for a given target geometry, between the gamma emission profile and the depth dose profile.

8 CONCLUSION

Prompt gamma emission detection is a promising means of range verification during proton therapy. It is the only current method that has the potential to provide *in situ* range information to clinicians and physicist without the complication of biological decay. While this technique is still in its infancy, we and others have shown that there is a correlation between the gamma emittance profile along the proton beam path and the proton depth dose profile. While inhomogeneities in the target geometry complicate matters, methods of filtering (namely, integrating fluence over a set photon energy range) greatly improves results.

There is still a great deal of work to be done before this becomes a clinically viable tool. Our studies have merely demonstrated a qualitative correlation between gamma emission profile and depth dose profile. Further studies must be conducted to develop a quantitative correlation. Experiments must verify that the simulated results are reproducible in a real-world setting, and further benchmarking must be conducted before the simulations can provide quantitative data that will be used for patient treatment assessment. In addition to the work at MGH, centers around the world are beginning to realize the potential of this technique, with significant contributions being made by Min and Kang *et al* at the National Cancer Center of Korea, and Polf *et al* at the MD Anderson Cancer Center. [Min, 2006] [Kang, 2009] [Polf, 2009]

While tackling these issues is no simple task, the potential benefits are well worth the work. Should the potential of this technique come to fruition to provide range verification during proton therapy, clinicians could reduce treatment planning margins, and errors that affect the proton beam range could be detected and corrected. If used clinically, this technique would spare healthy tissue while improving tumor conformality, ultimately improving the probability of a successful patient outcome.

REFERENCES

Belhout, A. *et al.* Gamma-ray production by proton and alpha particle induced reactions on ^{12}C, ^{16}O, ^{24}Mg, and Fe. *Physical Review C.* 2007 Sept; 76(3):034607-1 – 034607-19

Blomlie, V. *et al.* Female pelvic bone marrow: serial MR image before, during, and after radiation therapy. *Radiobiology.* 1995 Feb;194(2)537-43

Bortfeld, T. Heavy Charged Particles for Cancer Radiation Therapy. MIT Course HST.187 Lecture Notes. 2008

Cavenagh, EC. *Et al.* Hematopoietic marrow regeneration in pediatric patients undergoing spinal irradiation: MR depiction. *AJNR Am J Neuroradiology.* 1995 Mar;16(3):461-7

Cho, *et al.* Foundations of Medical imaging. John Wilen & Sons Inc. New York: 1993

Chen, *et al International Journal of Radiation Oncology and Biological Physics.* 48 (3):339. 2000

Dyer, P. *et al.* Cross sections relevant to gamma-ray astronomy: Proton induced reactions. *Physical Review C* 1981 May; 23(5): 1865-1882

Gierga, DP. Personal Communication. 2009

Guatelli, G. *et al.* Geant4 anthropomorphic phantoms: models of the human body for radiation protection studies. SPENVIS and Geant4 Workshop. Catholic University, Leuven, Belgium. 3-7 October 2005

Hall, EJ et al. Radiobiology for the Radiologist. Lippincott Williams & Wilkins. Philadelphia: 2006

International Commission on Radiation Units and Measurements (ICRU) (1989) Tissue Substitutes in Radiation Dosimetry and Measurement. Report #44.

International Commission on Radiation Units and Measurements (ICRU) (2008) Dosimetry Systems for Use in Radiation Processing. Report #80.

Jiang, H. *et al.* Simulation of organ-specific patient effective dose due to secondary neutrons in proton radiation treatment. *Phys Med Biol.* 50 (2005) 4337-4353

Johnson, E. Monte Carlo Model of a Low-Energy Neutron Interrogation Stsyem for Detecting Fissile Material. MS and BS Thesis. Massachusetts Institute of Technology. June 2006

Kang, B. *et al.* Monte Carlo design study of a gamma detector system to locate distal dose falloff in proton therapy. *IEEE Transactions on Nuclear Science.* Vol 56, No 1, 2009.

Kiener, J. *et al.* Gamma-ray production by inelastic proton scattering on ^{16}O and ^{12}C. *Physical Review C.* 1998 Oct; 58(4): 2174-2179

Knoll, G. Radiation Detection and Measurement. John Wiley & Sons Inc. New York: 2000

Knopf, A. et al. Quantitative assessment of the physical potential of proton beam range verification with PET/CT. Physics in Medicine and Biology. 53 (2008) 4137-4151

Krejcarek, SC *et al.* Physiologic and radiographic evidence of the distal edge of the proton beam in craniospinal irradiation. *International Journal of Radiation Oncology and Biological Physics.* 2007 Jul1; 68(3):646-9

Min, C. et al. Prompt gamma measurement for locating the dose falloff region in the proton therapy. Applied Physics Letters 80. 183517 (2006)

Mori, S. *et al.* Quantative assessment of range fluctuations in charged particle lung irradiation. *International Journal of Radiation Oncology and Biological Physics.* 2007 Oct 27 (1):308-17

Paganetti H and Gottschalk B (2003) Test of Geant3 and Geant4 nuclear models for 160 MeV protons stopping in CH2. *Med. Phys.* 30 1926-1931

Paganetti H *et al* (2008) Clinical implementation of Monte Carlo dose calculation in proton beam therapy. *Phys Med. Biol.* 53 4825-4853

Parodi K *et al.* (2007a) PET/CT imaging for treatment verification after proton therapy: a study with plastic phantoms and metallic implants. *Med. Phys.* 2007a;34:419-435.

Parodi K *et al.* (2007b) Patient study of in vivo verification of beam delivery and range, using PETand CT imaging after proton therapy. *Int. J. Radiat. Oncol. Biol. Phys.* 68 920-934.

Pelowitz, D. *et al.* MCNPX User's Manual. Loa Alamos National Labs. 2008

Polf, J. *et al.* Prompt gamma-ray emission from biological tissues during proton irradiation: a preliminary study. *Phys Med Biol* **54** (2009) 731-743

Turner, JE. Atoms, Radiation, and Radiation Protection. Wiley-VCH Verlag GmbH & Co. KGaG, Weinheim: 2004

Wilson, RR. (1946) Radiological Uses of Fast Protons. Radiology 47 487-491

Voet, D *et al.* Biochemistry. John Wiley & Sons Inc. New York: 1995

Yip, S. Neutron interactions and applications. MIT Course 22.106. Lecture Notes. 2006

APPENDIX A MONTE CARLO TECHNIQUES AND MCNP

Monte Carlo techniques use random numbers to simulate radiation transport through a given environment. An input deck is defined by the user and includes the geometry of the problem, the source position(s), spread, vector, etc., types and positions of tallies to be included, the cross sections to be referenced, and what types of physics are to be included (what particles are tracked, energy cutoff's, types of interactions to be considered etc.). The probability of a particle interacting over a given path distance is defined by the cross section, and by using random numbers between 0 and 1 and choosing the path length from the cumulative probability distribution, a sampling of the path lengths between collisions for a given particle are obtained. The same procedure is used to determine the type of interaction that may take place during a collision and the resulting particle(s) trajectory(s). [Yip, 2006]

Tallies use various means (time of flight, etc.) to determine the number of particles passing through a given cell or across a given surface, or to determine the amount of energy deposited in a given cell. Tallies are segmented by particle energy, energy deposited, particle angle, or time. The results are normalized to produce a quantity (particle fluence, MeV deposited, etc.) per source particle.

MCNP repeats this process for a given number of source particles and for each particle created via a collision or Bremsstrahlung (provided the new particle does not have an importance of zero, in which case it is not considered by MCNP). The results are summed and averaged, and error is estimated in the tallies based on the tally deviations. [Johnson, 2006]

APPENDIX B MCNPX ERROR: ENERGY BINNING

Given that MCNPX outputs tallies in a quantity-per-source-particle basis, one can not simply use Poisson statistics to determine the error associated with a given sample. For example, the NaI tallies outputted photon fluences from 0-20MeV with increments of 100keV (0.1MeV). However, in certain cases we wanted to only sample a small portion of this output, most often 4-5MeV. In order to obtain the total fluence, it was possible to simply sum the results for each energy in the desired range. Error, however, could not simply be summed. To complicate matters further, MCNP error is given as a relative error, where

$$MCNP\ relative\ error\ (RE) = \%\ Error$$

$$MCNP\ relative\ error = \frac{Std.\ Deviation}{Mean} = \frac{\sigma}{\mu}$$

We therefore obtain

$$\sigma = RE \bullet \mu$$

From this, we used the propagation of standard deviations

$$\sigma_{Total} = \sqrt{\sum_i \sigma_i^2}$$

we were able to determine the total standard deviation of the integral photon fluence for a given energy range.

APPENDIX C DETERMINING ANGULAR EMISSION OF GAMMAS IN GEANT

GEANT4.8.0 allows for particle by particle sampling, allowing us to simply set up an if statement for how to tally gammas. The geometry was set up as such:

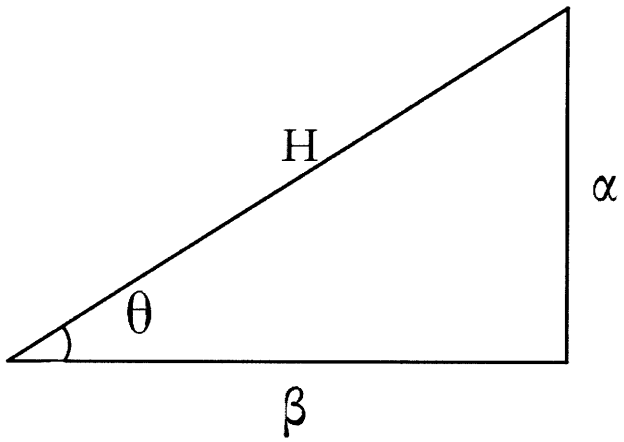

Where β is the path length taken in a photon's first step (after being created by the incident proton) along the **z** axis, which is the central axis of the proton beam, and α is the path length taken in a photon's first step in the **xy** plane.

$$\alpha = \sqrt{(x_1 - x_0)^2 + (y_1 - y_0)^2}$$
$$\beta = z_1 - z_0$$
$$H = \sqrt{\alpha^2 + \beta^2}$$

Where $\mathbf{r_0}$ is the position where the gamma is created, and $\mathbf{r_1}$ is the position of the gamma after it's first step. Therefore

$$\cos(\theta) = \frac{\beta}{H}$$
$$\cos(\theta) = \frac{z_1 - z_0}{\sqrt{(x_1 - x_0)^2 + (y_1 - y_0)^2 + (z_1 - z_0)^2}}$$

An if statement was written that tallied the cosine of each gamma produced (with respect to the central axis of the proton beam) provided it was created in the phantom and was created by the primary beam.

APPENDIX D SAMPLE MCNPX INPUTS

INPUT USED TO DETERMINE THE ANGULAR DISTRIBUTION OF THE GAMMAS EXITING THE LUCITE QA PHANTOM, E_{P+}=147.5MEV

```
C Cells
1 1 -1.19 1 -2 -100 imp:p=1 imp:n,H,e=1
2 0 2 -3 -100 imp:p=0 imp:n,H,e=1
3 1 -1.19 3 -4 -100 imp:p=1 imp:n,H,e=1
4 0 4 -5 -100 imp:p=0 imp:n,H,e=1
5 1 -1.19 5 -6 -100 imp:p=1 imp:n,H,e=1
6 0 6 -7 -100 imp:p=0 imp:n,H,e=1
7 1 -1.19 7 -8 -100 imp:p=1 imp:n,H,e=1
8 0 8 -9 -100 imp:p=0 imp:n,H,e=1
9 1 -1.19 9 -10 -100 imp:p=1 imp:n,H,e=1
10 0 10 -11 -100 imp:p=0 imp:n,H,e=1
11 1 -1.19 11 -12 -100 imp:p=1 imp:n,H,e=1
12 0 12 -13 -100 imp:p=0 imp:n,H,e=1
13 1 -1.19 13 -14 -100 imp:p=1 imp:n,H,e=1
14 0 14 -15 -100 imp:p=0 imp:n,H,e=1
15 1 -1.19 15 -16 -100 imp:p=1 imp:n,H,e=1
16 0 16 -17 -100 imp:p=0 imp:n,H,e=1
17 1 -1.19 17 -18 -100 imp:p=1 imp:n,H,e=1
18 0 18 -19 -100 imp:p=0 imp:n,H,e=1
19 1 -1.19 19 -20 -100 imp:p=1 imp:n,H,e=1
20 0 20 -21 -100 imp:p=0 imp:n,H,e=1
21 1 -1.19 21 -22 -100 imp:p=1 imp:n,H,e=1
22 0 22 -23 -100 imp:p=0 imp:n,H,e=1
23 1 -1.19 23 -24 -100 imp:p=1 imp:n,H,e=1
24 0 24 -25 -100 imp:p=0 imp:n,H,e=1
25 1 -1.19 25 -26 -100 imp:p=1 imp:n,H,e=1
26 0 26 -27 -100 imp:p=0 imp:n,H,e=1
27 1 -1.19 27 -28 -100 imp:p=1 imp:n,H,e=1
28 0 28 -29 -100 imp:p=0 imp:n,H,e=1
29 1 -1.19 29 -30 -100 imp:p=1 imp:n,H,e=1
30 0 30 -31 -100 imp:p=0 imp:n,H,e=1
31 1 -1.19 31 -32 -100 imp:p=1 imp:n,H,e=1
32 0 32 -33 -100 imp:p=0 imp:n,H,e=1
33 1 -1.19 33 -34 -100 imp:p=1 imp:n,H,e=1
34 0 34 -35 -100 imp:p=0 imp:n,H,e=1
35 1 -1.19 35 -36 -100 imp:p=1 imp:n,H,e=1
36 0 36 -37 -100 imp:p=0 imp:n,H,e=1
```

```
37 1 -1.19 37 -38 -100 imp:p=1 imp:n,H,e=1
38 0 38 -39 -100 imp:p=0 imp:n,H,e=1
39 1 -1.19 39 -40 -100 imp:p=1 imp:n,H,e=1
40 0 40 -41 -100 imp:p=0 imp:n,H,e=1
41 1 -1.19 41 -42 -100 imp:p=1 imp:n,H,e=1
42 0 42 -43 -100 imp:p=0 imp:n,H,e=1
43 1 -1.19 43 -44 -100 imp:p=1 imp:n,H,e=1
C
100 0 (-1:44:100) -999 imp:n,H,p,e=1
C
999 0 999 imp:n,H,p,e=0
C Blank Line

C Blank Line
C Surfaces
1 pz 0
2 pz 0.9995
3 pz 1.0005
4 pz 1.9995
5 pz 2.0005
6 pz 2.9995
7 pz 3.0005
8 pz 3.9995
9 pz 4.0005
10 pz 4.9995
11 pz 5.0005
12 pz 5.9995
13 pz 6.0005
14 pz 6.9995
15 pz 7.0005
16 pz 7.9995
17 pz 8.0005
18 pz 8.9995
19 pz 9.0005
20 pz 9.9995
21 pz 10.0005
22 pz 10.9995
23 pz 11.0005
24 pz 11.9995
25 pz 12.0005
26 pz 12.9995
27 pz 13.0005
28 pz 13.9995
29 pz 14.0005
30 pz 14.9995
31 pz 15.0005
```

```
32 pz 15.9995
33 pz 16.0005
34 pz 16.9995
35 pz 17.0005
36 pz 17.9995
37 pz 18.0005
38 pz 18.9995
39 pz 19.0005
40 pz 19.9995
41 pz 20.0005
42 pz 20.9995
43 pz 21.0005
44 pz 21.9995
C
100 cz 5
C
999 so 1000
C Blank Line

C Blank Line
mode n H p e
phys:H 150 0 -1 J 0 J 1
phys:e 100 1 1 1 1 0 0 0 0 0
phys:p 100 1 0 -1 1 0
sdef par=9 erg=147.5 pos=0 0 -.001 vec=0 0 1 dir=1
m1 1001 0.041959 6012 0.625017 8016 0.333024 $Lucite,
rho=1.190g/cc
f1:p (1 2) (3 4) (5 6) (7 8) (9 10) (11 12) (13 14) (15 16)
(17 18)
     (19 20) (21 22) (23 24) (25 26) (27 28) (29 30) (31 32)
(33 34)
     (35 36) (37 38) (39 40) (41 42) (43 44) $ Tally
ft1 frv 0 0 1 $ cosine taken WRT vector (0,0,1)
*c1 175 35i 0 $ cosine bin from 0-180deg w/ 5 deg increments
f11:p 100
ft11 frv 0 0 1
*c11 175 35i 0
fs11 -1 -2 -3 -4 -5 -6 -7 -8 -9 -10 -11 -12 -13 -14 -15 -16 -
17 -18
     -19 -20 -21 -22 -23 -24 -25 -26 -27 -28 -29 -30 -31 -32 -
33 -34 -35
     -36 -37 -38 -39 -40 -41 -42 -43 -44
f6:H 1 3 5 7 9 11 13 15 17 19 21 23 25 27 29 31 33 35 37 39 41
43
e6 0 25 50 75 100 125 150
nps 1000000
```

```
print
```

INPUT USED TO SIMULATE HOMOGENEOUS LUCITE QA PHANTOM, E_{p+}=147.5MEV

```
C QA Phantom
C Cells
1 1 -1.19 301 -302 -601 imp:p,H,e,n=1
2 1 -1.19 302 -303 -601 imp:p,H,e,n=1
3 1 -1.19 303 -304 -601 imp:p,H,e,n=1
4 1 -1.19 304 -305 -601 imp:p,H,e,n=1
5 1 -1.19 305 -306 -601 imp:p,H,e,n=1
6 1 -1.19 306 -307 -601 imp:p,H,e,n=1
7 1 -1.19 307 -308 -601 imp:p,H,e,n=1
8 1 -1.19 308 -309 -601 imp:p,H,e,n=1
9 1 -1.19 309 -310 -601 imp:p,H,e,n=1
10 1 -1.19 310 -311 -601 imp:p,H,e,n=1
11 1 -1.19 311 -312 -601 imp:p,H,e,n=1
12 1 -1.19 312 -313 -601 imp:p,H,e,n=1
13 1 -1.19 313 -314 -601 imp:p,H,e,n=1
14 1 -1.19 314 -315 -601 imp:p,H,e,n=1
15 1 -1.19 315 -316 -601 imp:p,H,e,n=1
16 1 -1.19 316 -317 -601 imp:p,H,e,n=1
17 1 -1.19 317 -318 -601 imp:p,H,e,n=1
18 1 -1.19 318 -319 -601 imp:p,H,e,n=1
19 1 -1.19 319 -320 -601 imp:p,H,e,n=1
20 1 -1.19 320 -321 -601 imp:p,H,e,n=1
21 1 -1.19 321 -322 -601 imp:p,H,e,n=1
22 1 -1.19 322 -323 -601 imp:p,H,e,n=1
23 1 -1.19 323 -324 -601 imp:p,H,e,n=1
24 1 -1.19 324 -325 -601 imp:p,H,e,n=1
25 1 -1.19 325 -326 -601 imp:p,H,e,n=1
26 1 -1.19 326 -327 -601 imp:p,H,e,n=1
27 1 -1.19 327 -328 -601 imp:p,H,e,n=1
28 1 -1.19 328 -329 -601 imp:p,H,e,n=1
29 1 -1.19 329 -330 -601 imp:p,H,e,n=1
30 1 -1.19 330 -331 -601 imp:p,H,e,n=1
31 1 -1.19 331 -332 -601 imp:p,H,e,n=1
32 1 -1.19 332 -333 -601 imp:p,H,e,n=1
33 1 -1.19 333 -334 -601 imp:p,H,e,n=1
34 1 -1.19 334 -335 -601 imp:p,H,e,n=1
35 1 -1.19 335 -336 -601 imp:p,H,e,n=1
36 1 -1.19 336 -337 -601 imp:p,H,e,n=1
37 1 -1.19 337 -338 -601 imp:p,H,e,n=1
```

```
38 1 -1.19 338 -339 -601 imp:p,H,e,n=1
39 1 -1.19 339 -340 -601 imp:p,H,e,n=1
40 1 -1.19 340 -341 -601 imp:p,H,e,n=1
41 1 -1.19 341 -342 -601 imp:p,H,e,n=1
C Collimators
50 0 301 -343 601 -602 imp:p,H,e,n=0
51 0 303 -344 601 -602 imp:p,H,e,n=0
52 0 305 -345 601 -602 imp:p,H,e,n=0
53 0 307 -346 601 -602 imp:p,H,e,n=0
54 0 309 -347 601 -602 imp:p,H,e,n=0
55 0 311 -348 601 -602 imp:p,H,e,n=0
56 0 313 -349 601 -602 imp:p,H,e,n=0
57 0 315 -350 601 -602 imp:p,H,e,n=0
58 0 317 -351 601 -602 imp:p,H,e,n=0
59 0 319 -352 601 -602 imp:p,H,e,n=0
60 0 321 -353 601 -602 imp:p,H,e,n=0
61 0 323 -354 601 -602 imp:p,H,e,n=0
62 0 325 -355 601 -602 imp:p,H,e,n=0
63 0 327 -356 601 -602 imp:p,H,e,n=0
64 0 329 -357 601 -602 imp:p,H,e,n=0
65 0 331 -358 601 -602 imp:p,H,e,n=0
66 0 333 -359 601 -602 imp:p,H,e,n=0
67 0 335 -360 601 -602 imp:p,H,e,n=0
68 0 337 -361 601 -602 imp:p,H,e,n=0
69 0 339 -362 601 -602 imp:p,H,e,n=0
70 0 341 -363 601 -602 imp:p,H,e,n=0
C NaI Detectors
100 2 -3.667 301 -303 602 -603 imp:n,H,e=1 imp:p=2
101 2 -3.667 303 -305 602 -603 imp:n,H,e=1 imp:p=2
102 2 -3.667 305 -307 602 -603 imp:n,H,e=1 imp:p=2
103 2 -3.667 307 -309 602 -603 imp:n,H,e=1 imp:p=2
104 2 -3.667 309 -311 602 -603 imp:n,H,e=1 imp:p=2
105 2 -3.667 311 -313 602 -603 imp:n,H,e=1 imp:p=2
106 2 -3.667 313 -315 602 -603 imp:n,H,e=1 imp:p=2
107 2 -3.667 315 -317 602 -603 imp:n,H,e=1 imp:p=2
108 2 -3.667 317 -319 602 -603 imp:n,H,e=1 imp:p=2
109 2 -3.667 319 -321 602 -603 imp:n,H,e=1 imp:p=2
110 2 -3.667 321 -323 602 -603 imp:n,H,e=1 imp:p=2
111 2 -3.667 323 -325 602 -603 imp:n,H,e=1 imp:p=2
112 2 -3.667 325 -327 602 -603 imp:n,H,e=1 imp:p=2
113 2 -3.667 327 -329 602 -603 imp:n,H,e=1 imp:p=2
114 2 -3.667 329 -331 602 -603 imp:n,H,e=1 imp:p=2
115 2 -3.667 331 -333 602 -603 imp:n,H,e=1 imp:p=2
116 2 -3.667 333 -335 602 -603 imp:n,H,e=1 imp:p=2
117 2 -3.667 335 -337 602 -603 imp:n,H,e=1 imp:p=2
118 2 -3.667 337 -339 602 -603 imp:n,H,e=1 imp:p=2
```

```
119 2 -3.667 339 -341 602 -603 imp:n,H,e=1 imp:p=2
C Void Area
998 0 -999
     #1 #2 #3 #4 #5 #6 #7 #8 #9 #10 #11
     #12 #13 #14 #15 #16 #17 #18 #19 #20 #21
     #22 #23 #24 #25 #26 #27 #28 #29 #30 #31
     #32 #33 #34 #35 #36 #37 #38 #39 #40 #41
     #50 #51 #52 #53 #54 #55 #56 #57 #58 #59
     #60 #61 #62 #63 #64 #65 #66 #67 #68 #69
     #70
     #100 #101 #102 #103 #104 #105 #106 #107
     #108 #109 #110 #111 #112 #113 #114 #115
     #116 #117 #118 #119
     imp:H,e,n=1 imp:p=2
999 0 999 imp:p,H,e,n=0
C Blank Line

C Blank Line
C Surfaces
C PX 101-199
C PY 201-299
C PZ 301-399
301 pz 0
302 pz 0.5
303 pz 1
304 pz 1.5
305 pz 2
306 pz 2.5
307 pz 3
308 pz 3.5
309 pz 4
310 pz 4.5
311 pz 5
312 pz 5.5
313 pz 6
314 pz 6.5
315 pz 7
316 pz 7.5
317 pz 8
318 pz 8.5
319 pz 9
320 pz 9.5
321 pz 10
322 pz 10.5
323 pz 11
324 pz 11.5
```

```
325 pz 12
326 pz 12.5
327 pz 13
328 pz 13.5
329 pz 14
330 pz 14.5
331 pz 15
332 pz 15.5
333 pz 16
334 pz 16.5
335 pz 17
336 pz 17.5
337 pz 18
338 pz 18.5
339 pz 19
340 pz 19.5
341 pz 20
342 pz 30
C
343 pz 0.001
344 pz 1.001
345 pz 2.001
346 pz 3.001
347 pz 4.001
348 pz 5.001
349 pz 6.001
350 pz 7.001
351 pz 8.001
352 pz 9.001
353 pz 10.001
354 pz 11.001
355 pz 12.001
356 pz 13.001
357 pz 14.001
358 pz 15.001
359 pz 16.001
360 pz 17.001
361 pz 18.001
362 pz 19.001
363 pz 20.001
C CX & C/X 401-499
C CY & C/Y 501-599
C CZ & C/Z 601-699
601 cz 5.1
602 cz 25.1
603 cz 26.1
```

```
C Spheres 901-999
999 so 150
C Everything Else 701-899
C Blank Line

C Blank Line
mode p H n e
phys:H 150 0 -1 J 0 J 1
phys:e 100 1 1 1 1 0 0 0 0 0
phys:p 100 1 0 -1 1 0
C
sdef par=9 erg=147.5 pos=0 0 -.01 vec=0 0 1 dir=1
m1 1001 0.041959 6012 0.625017 8016 0.333024 $Lucite,
rho=1.190g/cc
m2 11023 0.153373 53123 0.846627 $NaI, rho=3.667g/cc
C
e6 0 25 50 75 100 125 150
fc6 Dose Deposited by p+ (for DD Curve)
f6:H 1 2 3 4 5 6 7 8 9 10 11 12 13 14 15 16 17 18 19 20
     21 22 23 24 25 26 27 28 29 30 31 32 33 34 35 36 37 38 39
40 41
e4 0 29i 150
fc4 p+ fluence
f4:H 1 2 3 4 5 6 7 8 9 10 11 12 13 14 15 16 17 18 19 20
     21 22 23 24 25 26 27 28 29 30 31 32 33 34 35 36 37 38 39
40 41
e14 0 199i 20
fc14 Gamma Fluence in NaI Detectors
f14:p 100 101 102 103 104 105 106 107 108 109 110 111 112 113
114
     115 116 117 118 119
C
nps 100000
print
```

INPUT USED TO SIMULATE HETEROGENEOUS PHANTOM, E_{p+}=147.5MEV, LUNG → BONE

```
C Inhomogeneous Phantom
C Cells
C Dose Cylinders
1 3 -0.3 -301 302 -601 imp:p,H,e,n=1
2 3 -0.3 -302 303 -601 imp:p,H,e,n=1
3 3 -0.3 -303 304 -601 imp:p,H,e,n=1
4 3 -0.3 -304 305 -601 imp:p,H,e,n=1
```

```
5 3 -0.3 -305 306 -601 imp:p,H,e,n=1
6 3 -0.3 -306 307 -601 imp:p,H,e,n=1
7 3 -0.3 -307 308 -601 imp:p,H,e,n=1
8 3 -0.3 -308 309 -601 imp:p,H,e,n=1
9 3 -0.3 -309 310 -601 imp:p,H,e,n=1
10 3 -0.3 -310 311 -601 imp:p,H,e,n=1
11 3 -0.3 -311 312 -601 imp:p,H,e,n=1
12 3 -0.3 -312 313 -601 imp:p,H,e,n=1
13 3 -0.3 -313 314 -601 imp:p,H,e,n=1
14 3 -0.3 -314 315 -601 imp:p,H,e,n=1
15 3 -0.3 -315 316 -601 imp:p,H,e,n=1
16 3 -0.3 -316 317 -601 imp:p,H,e,n=1
17 2 -1.82 -317 318 -601 imp:p,H,e,n=1
18 2 -1.82 -318 319 -601 imp:p,H,e,n=1
19 2 -1.82 -319 320 -601 imp:p,H,e,n=1
20 2 -1.82 -320 321 -601 imp:p,H,e,n=1
21 2 -1.82 -321 322 -601 imp:p,H,e,n=1
22 2 -1.82 -322 323 -601 imp:p,H,e,n=1
23 2 -1.82 -323 324 -601 imp:p,H,e,n=1
24 2 -1.82 -324 325 -601 imp:p,H,e,n=1
25 2 -1.82 -325 326 -601 imp:p,H,e,n=1
26 2 -1.82 -326 327 -601 imp:p,H,e,n=1
27 2 -1.82 -327 328 -601 imp:p,H,e,n=1
28 2 -1.82 -328 329 -601 imp:p,H,e,n=1
29 2 -1.82 -329 330 -601 imp:p,H,e,n=1
30 2 -1.82 -330 331 -601 imp:p,H,e,n=1
31 2 -1.82 -331 332 -601 imp:p,H,e,n=1
32 2 -1.82 -332 333 -601 imp:p,H,e,n=1
33 2 -1.82 -333 334 -601 imp:p,H,e,n=1
34 2 -1.82 -334 335 -601 imp:p,H,e,n=1
35 2 -1.82 -335 336 -601 imp:p,H,e,n=1
36 2 -1.82 -336 337 -601 imp:p,H,e,n=1
37 2 -1.82 -337 338 -601 imp:p,H,e,n=1
38 2 -1.82 -338 339 -601 imp:p,H,e,n=1
39 2 -1.82 -339 340 -601 imp:p,H,e,n=1
40 2 -1.82 -340 341 -601 imp:p,H,e,n=1
41 2 -1.82 -341 342 -601 imp:p,H,e,n=1
C
C Collimators
50 0 -301 343 602 -603 imp:p,H,e,n=0
51 0 -303 344 602 -603 imp:p,H,e,n=0
52 0 -305 345 602 -603 imp:p,H,e,n=0
53 0 -307 346 602 -603 imp:p,H,e,n=0
54 0 -309 347 602 -603 imp:p,H,e,n=0
55 0 -311 348 602 -603 imp:p,H,e,n=0
56 0 -313 349 602 -603 imp:p,H,e,n=0
```

```
57 0 -315 350 602 -603 imp:p,H,e,n=0
58 0 -317 351 602 -603 imp:p,H,e,n=0
59 0 -319 352 602 -603 imp:p,H,e,n=0
60 0 -321 353 602 -603 imp:p,H,e,n=0
61 0 -323 354 602 -603 imp:p,H,e,n=0
62 0 -325 355 602 -603 imp:p,H,e,n=0
63 0 -327 356 602 -603 imp:p,H,e,n=0
64 0 -329 357 602 -603 imp:p,H,e,n=0
65 0 -331 358 602 -603 imp:p,H,e,n=0
66 0 -333 359 602 -603 imp:p,H,e,n=0
67 0 -335 360 602 -603 imp:p,H,e,n=0
68 0 -337 361 602 -603 imp:p,H,e,n=0
69 0 -339 362 602 -603 imp:p,H,e,n=0
70 0 -341 363 602 -603 imp:p,H,e,n=0
C
C NaI Detectors
100 4 -3.667 -301 303 603 -604 imp:n,H,e=1 imp:p=2
101 4 -3.667 -303 305 603 -604 imp:n,H,e=1 imp:p=2
102 4 -3.667 -305 307 603 -604 imp:n,H,e=1 imp:p=2
103 4 -3.667 -307 309 603 -604 imp:n,H,e=1 imp:p=2
104 4 -3.667 -309 311 603 -604 imp:n,H,e=1 imp:p=2
105 4 -3.667 -311 313 603 -604 imp:n,H,e=1 imp:p=2
106 4 -3.667 -313 315 603 -604 imp:n,H,e=1 imp:p=2
107 4 -3.667 -315 317 603 -604 imp:n,H,e=1 imp:p=2
108 4 -3.667 -317 319 603 -604 imp:n,H,e=1 imp:p=2
109 4 -3.667 -319 321 603 -604 imp:n,H,e=1 imp:p=2
110 4 -3.667 -321 323 603 -604 imp:n,H,e=1 imp:p=2
111 4 -3.667 -323 325 603 -604 imp:n,H,e=1 imp:p=2
112 4 -3.667 -325 327 603 -604 imp:n,H,e=1 imp:p=2
113 4 -3.667 -327 329 603 -604 imp:n,H,e=1 imp:p=2
114 4 -3.667 -329 331 603 -604 imp:n,H,e=1 imp:p=2
115 4 -3.667 -331 333 603 -604 imp:n,H,e=1 imp:p=2
116 4 -3.667 -333 335 603 -604 imp:n,H,e=1 imp:p=2
117 4 -3.667 -335 337 603 -604 imp:n,H,e=1 imp:p=2
118 4 -3.667 -337 339 603 -604 imp:n,H,e=1 imp:p=2
119 4 -3.667 -339 341 603 -604 imp:n,H,e=1 imp:p=2
C
C Inhomogeneous Phantom
201 1 -1.18 -701 imp:p,H,e,n=1
202 1 -1.18 -702 imp:p,H,e,n=1
203 1 -1.18 -703 imp:p,H,e,n=1
204 1 -1.18 -704 imp:p,H,e,n=1
205 1 -1.18 -705 imp:p,H,e,n=1
206 1 -1.18 -706 imp:p,H,e,n=1
207 2 -1.82 -707 imp:p,H,e,n=1
208 2 -1.82 -708 #17 #18 #19 #20 #21 #22 #23
```

```
                #24 #25 #26 #27 #28 #29 #30
                #31 #32 #33 #34 #35 #36 #37
                #38 #39 #40 #41 imp:p,H,e,n=1
209 3 -.3 -709 imp:p,H,e,n=1
210 3 -.3 -710 #1 #2 #3 #4 #5 #6 #7 #8 #9 #10
              #11 #12 #13 #14 #15 #16 imp:p,H,e,n=1
C
998 0 #1 #2 #3 #4 #5 #6 #7 #8 #9 #10 #11 #12
      #13 #14 #15 #16 #17 #18 #19 #20 #21 #22
      #23 #24 #25 #26 #27 #28 #29 #30 #31 #32
      #33 #34 #35 #36 #37 #38 #39 #40 #41
      #50 #51 #52 #53 #54 #55 #56 #57 #58 #59
      #60 #61 #62 #63 #64 #65 #66 #67 #68 #69 #70
      #100 #101 #102 #103 #104 #105 #106 #107
      #108 #109 #110 #111 #112 #113 #114 #115
      #116 #117 #118 #119
      #201 #202 #203 #204 #205 #206 #207 #208 #209 #210 -999
     imp:p,H,e,n=1
999 0 999 imp:p,H,e,n=0
C Blank Line

C Blank Line
C Surfaces
C PX 101-199
C PY 201-299
C PZ 301-399
301 pz 11.15
302 pz 10.65
303 pz 10.15
304 pz 9.65
305 pz 9.15
306 pz 8.65
307 pz 8.15
308 pz 7.65
309 pz 7.15
310 pz 6.65
311 pz 6.15
312 pz 5.65
313 pz 5.15
314 pz 4.65
315 pz 4.15
316 pz 3.65
317 pz 3.55
318 pz 3.05
319 pz 2.55
320 pz 2.05
```

```
321 pz 1.55
322 pz 1.05
323 pz 0.55
324 pz 0.05
325 pz -0.45
326 pz -0.95
327 pz -1.45
328 pz -1.95
329 pz -2.45
330 pz -2.95
331 pz -3.45
332 pz -3.95
333 pz -4.45
334 pz -4.95
335 pz -5.45
336 pz -5.95
337 pz -6.45
338 pz -6.95
339 pz -7.45
340 pz -7.95
341 pz -8.45
342 pz -8.95
C
343 pz 11.149
344 pz 10.149
345 pz 9.149
346 pz 8.149
347 pz 7.149
348 pz 6.149
349 pz 5.149
350 pz 4.149
351 pz 3.549
352 pz 2.549
353 pz 1.549
354 pz 0.549
355 pz -0.451
356 pz -1.451
357 pz -2.451
358 pz -3.451
359 pz -4.451
360 pz -5.451
361 pz -6.451
362 pz -7.451
363 pz -8.451
C CX & C/X 401-499
C CY & C/Y 501-599
```

```
C CZ & C/Z 601-699
601 c/z -6.4 .45 1
602 cz 16
603 cz 26
604 cz 27
C Everything Else 701-899
701 RPP -10.85 10.85  -8.85 -3.85  -13 13
702 RPP -13 13  -3.85 -1.55  -13 13
703 RPP 11.15 12.4  -1.55 2.45  -11.15 11.15
704 RPP -12.4 -11.15  -1.55 2.45  -11.15 11.15
705 RPP -11.15 11.15  2.45 3.65  -11.15 11.15
706 ARB 13 3.65 -13  13 3.65 13  13 8.85 -13  13 8.45 13
        -13 3.65 13  -13 3.65 -13  -13 8.85 13  -13 8.85 -13
        1234 1368 2457 1265 7834 5678
709 ARB 11.15 -1.55 3.25  11.15 -1.55
        11.15  11.15 2.45 3.75  11.15 2.45 11.15
        1.75 -1.55 3.25  1.75 -1.55 11.15
        1.25 2.45 3.75  1.25 2.45 11.15
        1234 5678 1537 2648 1526 3748
708 RPP -11.15 -1.65  -1.55 2.45  -11.15 3.55
707 ARB 11.15 -1.55 -16.15  11.15 -1.55 3.25
        11.15 2.45 -16.15  11.15 2.45 3.75
        1.75 -1.55 -16.15  1.75 -1.55 3.25
        1.25 2.45 -16.15  1.25 2.45 3.75
        1234 5678 1537 2648 1526 3748
710 RPP -11.15 -1.65  -1.55 2.45  3.55 11.15
C Spheres 901-999
999 so 200
C Blank Line

C Blank Line
mode p H n e
phys:H 150 0 -1 J 0 J 1
phys:e 100 1 1 1 1 0 0 0 0 0
phys:p 100 1 0 -1 1 0
sdef par=9 erg=147.5 pos=-6.4 0.45 11.2 vec=0 0 -1 dir=1
m1 1001 .0805 6012 .5999 8016 .3196 $ PMMA, rho=1.18 g/cc
m2 1001 .0341 6012 .3141 7014 .0184 8016 .3650
      17000 .0004 20000 .2681 $ Bone Eq., rho=1.82 g/cc
m3 1001 .0846 6012 .5938 7014 .0196 8016 .1814
      12000 .1119 17000 .0010 14000 .0078 $ Lung Eq., rho=0.30
g/cc
m4 11023 0.153373 53123 0.846627 $NaI, rho=3.667g/cc
C
e6 0 25 50 75 100 125 150
fc6 Dose Deposited by p+ (for DD Curve)
```

```
f6:H 1 2 3 4 5 6 7 8 9 10 11 12 13 14 15 16 17 18 19 20
     21 22 23 24 25 26 27 28 29 30 31 32 33 34 35 36 37 38 39
40 41
e4 0 29i 150
fc4 p+ fluence
f4:H 1 2 3 4 5 6 7 8 9 10 11 12 13 14 15 16 17 18 19 20
     21 22 23 24 25 26 27 28 29 30 31 32 33 34 35 36 37 38 39
40 41
e14 0 199i 20
fc14 Gamma Fluence in NaI Detectors
f14:p 100 101 102 103 104 105 106 107 108 109 110 111 112 113
114
     115 116 117 118 119
C
nps 100000000
print
```